

Complex patterns of schist tor exposure and surface uplift, Otago (New Zealand)

Gerald Raab^{a,*}, Adam P. Martin^b, Kevin P. Norton^c, Marcus Christl^d, Fabio Scarciglia^e, Markus Egli^a

^a Department of Geography, University of Zurich, Winterthurerstrasse 190, 8057 Zurich, Switzerland

^b GNS Science, Private Bag 1930, Dunedin, New Zealand

^c School of Geography, Environment and Earth Sciences, Te Herenga Waka, Victoria University of Wellington, PO Box 600, 6140 Wellington, New Zealand

^d Department of Physics, Laboratory of Ion Beam Physics, ETH Zürich, Otto-Stern-Weg 5, 8093 Zürich, Switzerland

^e Department of Biology, Ecology and Earth Sciences (DiBEST), University of Calabria, Via P. Bucci – Cubo 15B, 87036 Arcavacata di Rende, CS, Italy

ARTICLE INFO

Article history:

Received 22 March 2021

Received in revised form 30 June 2021

Accepted 4 July 2021

Available online 7 July 2021

Keywords:

Surface denudation

Erosion

Surface uplift

In situ ¹⁰Be

Tor formation

ABSTRACT

Landscapes are subjected to surface denudation during their complex and non-linear evolution. In order to quantify the in situ surface lowering and, thus, denudation or soil erosion rates, new, multi-millennia archives are needed and must be rigorously tested. Large residual rocks, tors, are the basis for the Tor Exhumation Approach. Here we present novel results on meta-sedimentary (schist) rock tors using this approach, which previously has only been applied in granitic terrains. The exhumation patterns of eight schist tors in three landscape locations (valley, ridge, distal) of Otago, New Zealand, were studied using cosmogenic dating. The in situ ¹⁰Be ages have high variability along individual vertical tor profiles. Average surface age is 122 ± 12 ka and ranges from 836 ± 89 ka to 19 ± 2 ka. The majority of investigated tors have surfaced during the MIS 5 which was one of the wettest and warmest climate periods. The resulting surface denudation trend of the three locations differs. The valley commenced denudation no earlier than ~ 200 ka with rates of -0.22 [m kyr⁻¹] to -0.02 [m kyr⁻¹]. In contrast, exposure started at the ridge position around 230 ka at -0.03 [m kyr⁻¹]. An age inversion found in the valley is considered to be the result of mushroom-like exposure by undercutting and repeated rock breakoffs. The distal site tor has been exhumed continuously for ~ 120 ka at a rate of -0.2 to -0.05 [m kyr⁻¹]. We identified a mix of surface emergence patterns of the tors such as continuous-, mushroom-, tafoni- and structural-like. The comparison to modern erosion rates indicates that surface erosion has increased up to a factor of ten during the last few decades. To determine the actual surface uplift, we linked the tor derived surface denudation rates with rock uplift data. The data indicates that the surface uplift rates started to decrease during the Middle Pleistocene (0.04 – 0.09 [m kyr⁻¹]), remained relatively low during the Late Pleistocene (~ 0.01 [m kyr⁻¹]) and started to increase again during the Holocene ($c. 0.21$ – 0.64 [m kyr⁻¹]). In summary, the emergence pattern of local tors enabled reconstruction of the evolution of Pleistocene-Holocene surfaces in East Otago.

© 2021 The Authors. Published by Elsevier B.V. This is an open access article under the CC BY license (<http://creativecommons.org/licenses/by/4.0/>).

1. Introduction

Earth's surfaces have evolved and reshaped over billions of years. Once primary mineral assemblages are exposed, chemical weathering begins to transform them into neogenic phases (e.g. clay minerals, iron oxyhydroxides). The continuous weathering of bedrock (W) and later removal by erosion (E) causes landscape surfaces to be denuded (D_{surface} ; [m yr⁻¹]) over time. In some cases, aeolian input (A) counteracts this process.

$$D_{\text{surface}} = W + E - A \quad (1)$$

The spatial and temporal variations of surface forming processes often result in a complex and non-linear landscape evolution history. Modern geomorphology aims at comprehending these past processes to understand present landscapes and predict their future evolution. With the use of geochronological methods (e.g. surface exposure dating, burial dating, isotope decay counting), time fragments of landscape evolution can be deciphered. A major challenge for deciphering past landscape histories is quantification of surface lowering processes at the denudational zone itself. Commonly, intra-terrain or terminal depositional zones are used to determine D_{surface} rates where the deposited material has originated from (e.g. Wittmann et al., 2007).

* Corresponding author.

E-mail address: gerald.raab@geo.uzh.ch (G. Raab).

The new Tor Exhumation Approach (TEA) by Raab et al. (2018, 2019) and Raab (2019) enables the analysis of surface evolution history over continuous time spans, up to the Pleistocene. The TEA is an investigation technique which also includes a modelling aspect. The TEA uses vertical in situ terrestrial cosmogenic nuclide (TCN) profiles along tors, i.e. large residual rocks that are still rooted in bedrock, to determine the often-multi-step exhumation record. The individual exhumation rates are converted to surface lowering rates for the surrounding landscape.

In general, tors are residual parts of the bedrock that resisted chemical and physical weathering (Linton, 1955). These bedrock remnants are often prominent and spectacular elements of today's landscapes with their often-vertical rock faces, and weathered joints. Over the last decades, tors have been the focus of four main research topics: timing and formation mechanisms of tors (Wood, 1969; Scarciglia et al., 2005; Gunnell et al., 2013), connection of bedrock structure and landform (Gibbons, 1981; Ehlen, 1992; Goodfellow et al., 2014), protection and preservation of tor landforms (Hättestrand and Stroeven, 2002; Hall and Migoñ, 2010; Evans et al., 2017) and tors as paleoenvironmental archives (e.g. Hall et al., 2015; Evans et al., 2017; Raab et al., 2018; Michniewicz, 2019).

Studies suggest boulders and tors of magmatic origin (e.g. granite, tonalite) are the result of deep spheroidal weathering (Migoñ, 2006). There is increasing evidence that supports the deep (about 15–20 m below the past topographic surface) formation of tors from selective saprolite formation due to preferential water flow pathways (Scarciglia et al., 2005). Current data show that chemical weathering at various depths is responsible for the progressive formation of subspherical cores (e.g. Ollier, 2010). Water flow is concentrated in initially sharp rock joints around the core stones. The joints are smoothed, widened and deepened over time. The subspherical rock cores emerge as tors and boulders once erosion removes the more mobile saprolite material adjacent and overlying them (Raab et al., 2018). Once the tor has been exhumed, physical weathering processes may become more intense, allowing surface exfoliation, sliding or rock fracturing. Most recently, conceptual models of how rounded conglomerate towers evolve have been developed (Migoñ, 2020). Some concepts on schist tor-formation currently lack behind but there is a developed understanding of saprolite formation in schist rock (e.g. Stolt et al., 1991; Craw and Kerr, 2017). The lateral variability in soil and saprolite horizons increases as schist rock dip increases and shearing or intrusion zones also help shape saprolite formation (Stolt and Baker, 1994). It is hypothesised that the variability in saprolite properties and characteristics are due to inherent differences within the structure, fabric, composition and grain size of the parent rock (Stolt and Baker, 1994).

Hence, tor formation processes in meta-sedimentary schist rock areas might differ compared to magmatic rock areas depending on the constituent rock fabric and bulk density. In general, textures in granite rocks are medium- to coarse-grained porphyritic (i.e. big and small) or equigranular. Textures in sedimentary rocks can be similar to textures in granitic rocks, i.e. a mudstone or a sandstone is equigranular or a conglomerate is equivalent to a porphyritic texture (big and small). Differences occur when a tectonic foliation introduces an anisotropic fabric versus an unfoliated, isotropic fabric. The structural isotropic fabric of granite develops in the final cooling stage, once the magma has consolidated. Its surface exposure can be the result of either edaphic alteration or by tectonic processes, with the later also resulting in a secondary fabric (Vidal Romani, 2008).

In contrast, the primary fabric of most meta-sedimentary rocks is produced during deposition, the secondary fabric by deformation. During diagenesis, the grain size, grain shape and compaction process control the intergranular spaces (i.e. void or cemented). Poorly cemented sediments can result in predisposing channels for meteoric agents, which in turn influence weathering pathways. The key factor controlling infiltration is the degree of compaction which is determined by the rock bulk density. The bulk density of meta-sedimentary rocks (~ 2.65 [g cm⁻³]; Hatherton and Leopard, 1964) overlaps with the lower range of granite (typically ~ 2.65 to ~ 2.75 [g cm⁻³]).

Foliation patterns in meta-sedimentary rocks can also redirect the gravity driven process of water flow, and therefore change a critical factor of tor formation. Also, the degradation of tors through detachment of rock slabs according to rock fabric and texture, instead of gradual surface lowering mechanisms (e.g. weathering, erosion), may complicate the schist tor formation process. Therefore, applying the TEA in foliated rock environments could potentially result in different and more abrupt exposure patterns. Up to now, the TEA has solely been applied in upland plateaus with gentle rolling paleosurfaces and unfoliated, magmatic (granitic) rock tors (Heimsath et al., 2001; Raab et al., 2018, 2019; Raab, 2019). Thus, the potential and limitation of the TEA for different lithologies and landscape settings still requires investigation.

This study focuses on the application of the TEA on foliated, meta-sedimentary (schist) rock tors in the horst and graben setting of the Otago plateau, South Island, New Zealand. This area experiences sharp gradients in rainfall. We will investigate denudation rate differences between a valley site (potential sediment sink) and an adjacent ridge site (continuous erosion and source of sediments). These two sites are also compared to a flat, distal site. The Otago plateau setting facilitates consideration of a distinct difference in tor exhumation rates and subsequent denudation rates, relative to magmatic (granitic) settings. Specifically, we will discuss schist tor and Otago landscape surface ages, schist tor formation patterns, make a comparison between surface and modern erosion patterns, investigate a surface denudation link with climate and consider the potential relationship between surface uplift and tor exposure. The results of this study will improve understanding of tor formation in foliated, meta-sedimentary lithologies and investigate the wider application of the TEA method.

2. Study area

The Otago Province study area is situated in the south-east of the South Island of New Zealand. Generally, slight to moderate surface erosion rates (Fig. 1a) are balanced by tectonic uplift rates of about 0–1 [mm yr⁻¹] (Fig. 1b). The Torlesse Terrane stretches across the Haast Schist (Fig. 1c) and greywacke basement rock terranes of the South Island and contains a large variety of schist tor morphologies and sizes within North and East Otago (Wood, 1969). The cavernously weathered tor surfaces and weathering pits of up to 1 m in diameter (most are ~ 10 – 20 cm; Fahey, 1986) on detached blocks around the base of many tors indicate that past periods of chemical weathering have been instrumental in the development of schist tors in Central Otago (Fahey, 1981). Their typically columnar or blocky form is controlled by sub-vertical jointing and sub-horizontal schistosity (Stirling, 1991). Local tors have prominent steep planar faces that mostly exceed 75° (summit tors; Old Man Range and Pisa Range; Fahey, 1981). Schist tors crop out in linear rows, and the trend of these linear exposures is NW to NNW (Turner, 1952). Stirling (1990) observed that tors most commonly occur in areas of strong concave-upwards flexure of peneplain surfaces, but tors also occur away from these surfaces. Local tors are seen as salients of schist rock remaining after erosion of the saprolite zone (Stirling, 1991; Wood, 1969; Fahey, 1981). It is suggested that the saprolite zone developed as an ongoing process from the Miocene, with similar but weaker processes ongoing up to the Pleistocene (Chamberlain et al., 1999; Craw et al., 2015). Since tors tend to be absent from extensive glaciated surfaces (e.g. Garvie Mountains), they have not formed after or during glacial modifications. Subsequently, tors on uplands and lowlands have likely formed from erosion of the pre-Quaternary saprolite zone. For the upland tors, primary aeolian and freeze-thaw erosion are considered as erosion factors (Stirling, 1991). The main erosion process for the low-land tors is still debated.

The tors in the study area are predominantly schist rock, part of the Otago Schist (Martin et al., 2016b). The rocks have been extensively metamorphosed and deformed and are part of the broader Haast Schist that occurs widely across New Zealand (Suggate, 1961). The schist can be subdivided based on textural classification. The textural zones are

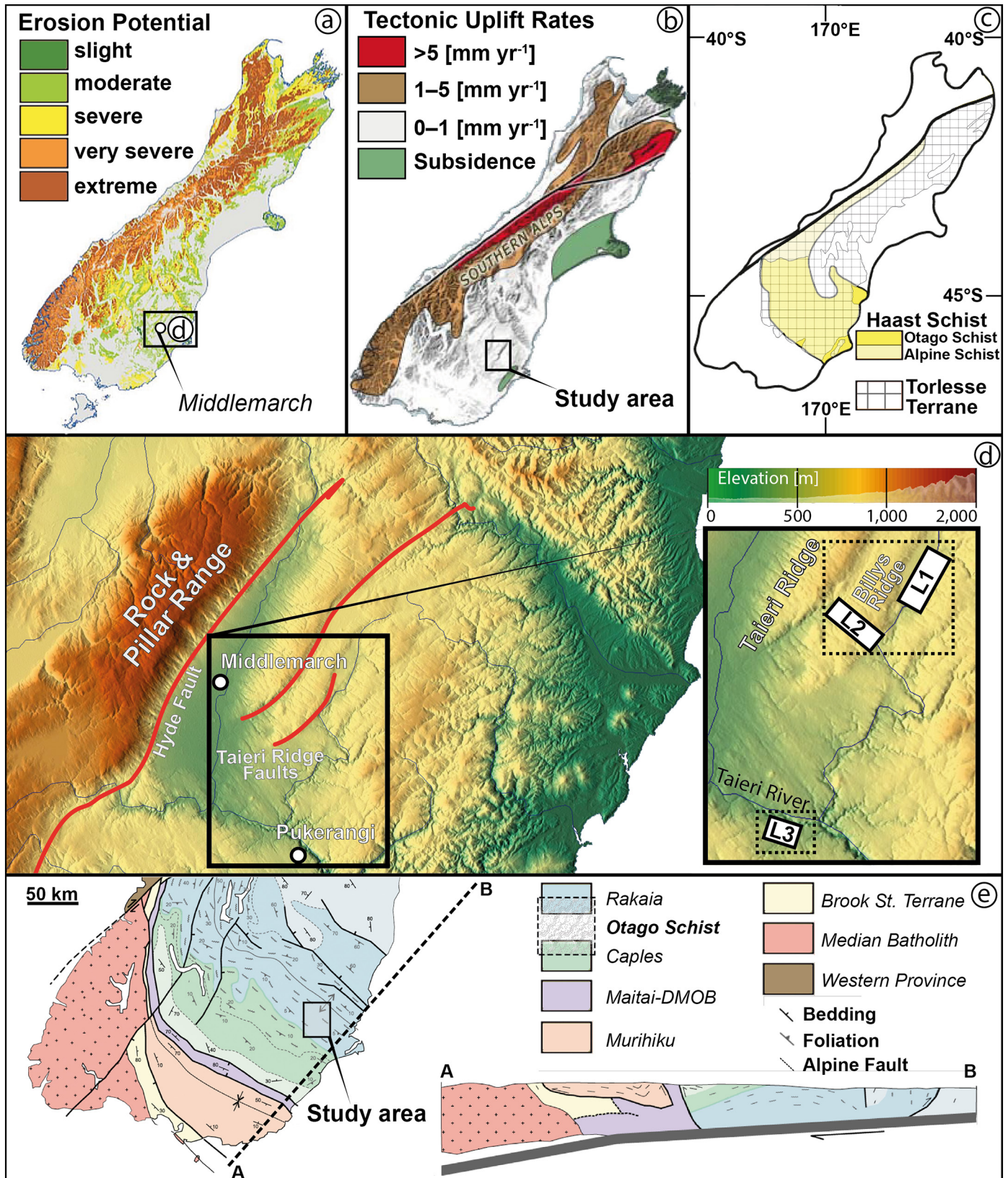


Fig. 1. Location and setting of the study area. (a) Potential soil erosion risk map of New Zealand modified after Basher (2010). (b) Tectonic uplift rates of the South Island, New Zealand (McSaveney and Nathan, 2006). (c) Torlesse Terrane of the South Island of New Zealand (after Weinberger et al., 2010; Mortimer and Cooper, 2004; Forster and Lister, 2003) (d) Digital elevation model of East Otago coloured by elevation. The red lines indicate major fault traces (Norris, 2004). The three study locations are indicated as L1 (valley location), L2 (ridge location) and L3 (off-site location). (e) Geological overview and cross-section of the study region (Mortimer et al., 2012). St. = Street. DMOB = Dun Mountain Ophiolite Belt. The digital elevation model was originally created by Geographx (geographx.co.nz) and was primarily derived from January 2012 LINZ Topo50 20 m contours (data.linz.govt.nz/layer/768) and sourced here: <https://data.linz.govt.nz/layer/51768-nz-8m-digital-elevation-model-2012>.

separated based upon mineral assemblage-defined metamorphic zones (Mortimer, 2000) or by isotoets which bound rocks with an equal development of mineral size, tectonic fabric, degree of foliation and segregation development (Turnbull et al., 2001). Otago Schist in the study area is entirely within the greenschist facies (garnet-biotite-albite zone) and textural zone IV, which encompasses the most highly deformed, well foliated and thickly segregated rocks (Martin et al., 2016b).

The tors in this study are compositionally monotonous quartzofeldspathic greyschist rocks. Subtle variations in modal abundance of constituent minerals in outcrop is seen as differences in colour and grain size, accentuated by varying foliation intensity (Martin et al., 2016b). Pervasive jointing is common (Weinberger et al., 2010) and are often abraded with highly developed tafoni, weathering pits and cave like structures (Brown, 1963). Both a mica (north-northwest–south-southeast) and a quartz (northwest-southeast) and lineation are strongly developed as crenulation axes or rods, respectively (Martin et al., 2016b). The mineralogy is dominated by quartz, albite, muscovite, epidote, chlorite, actinolite and stilpnomelane, with trace amounts of titanite (Martin et al., 2013). Accessory amounts of biotite, apatite, garnet, tourmaline, zircon, pyrite, graphite, marcasite and chalcopyrite have also been described from greyschist in the area (Brown, 1963, 1967).

These schistose rocks have been assigned to the Rakaia Terrane of the Torlesse Composite Terrane (or Supergroup) by lithology and geochemistry (Mortimer and Roser, 1992). The depositional age of the Rakaia Terrane by fossils and detrital zircon studies is mostly Permian to Triassic (Campbell and Warren, 1965; Turnbull, 2000; Adams et al., 2007, 2009), although local occurrences of schist with maximum Jurassic ages do occur in northwest Otago (Jugum et al., 2013). Peak metamorphism in the Otago Schist is thought to have occurred during the Jurassic (Little et al., 1999; Gray and Foster, 2004).

Our sampling sites are positioned in the hilly (11–25° slope angle) East Otago plateau (Fig. 1a,d) at an altitude of 300 m a.s.l. and above (Table 1), part of the larger Torlesse Terrane (Fig. 1e). The valley (Billys Flat) and the ridge (Billys Ridge) are also compared to a flat, distal location (Pukerangi) on the south-west side of the Taieri River (Fig. 2a). The Pukerangi site is ~1 km from a gorge. All three sites are part of the Rakaia Terrane in East Otago. The distal site is the closest location to the Caples Terrane (Fig. 1d,e; Mortimer, 2004).

The average, near surface north-westerly wind speeds of 30–60 [km h⁻¹] reach maxima of 130 [km h⁻¹] at altitudes below 1000 m a.s.l. (McGowan and Sturman, 1996). The high wind speeds are the result of periodic events (e.g. foehn wind of the Southern Alps) and topographic channelling (e.g. mountains, hills; McGowan et al., 2002). In general, the Otago climate is characterised as one of the driest, most continental areas in New Zealand (Maunder, 1965). The semi-arid conditions reach precipitation lows of about 300–350 [mm yr⁻¹] in the inland areas of Otago at altitudes below c. 550 m a.s.l. (Cossens, 1987), which is the highest altitude site in this study.

The Taieri Ridge region is characterised by an annual precipitation of about 600 [mm yr⁻¹] coupled with wind-driven evaporation that exceeds rainfall, causing partial salt encrustations on tors (Craw and Beckett, 2004). The study area has never experienced Quaternary glaciations (Wood, 1969; Barrell, 2011).

3. Materials and methods

3.1. Overview

Sampling procedure outlined in Raab et al. (2018, 2019) and Raab (2019) include the vertical profile sampling of tors and chemical extraction of TCN (¹⁰Be). The measured contents are blank corrected and converted to surface ages. By using Monte Carlo simulations, various exhumation trends are modelled within the age variations. The mathematical derivations of these functions are used to model surface denudation (D_{Surface}). In addition, modern soil erosion rates determined by fallout radionuclides (¹³⁷Cs) are used as reference (Hewitt, 1996; Basher, 2000).

3.2. Sampling procedure for in situ ¹⁰Be surface exposure dating

We have investigated three tors at the Billys flat valley, four tors at the adjacent Billys ridge and one tor at a distal location at Pukerangi (Fig. 2a,b,c,d). All eight tors have a minimum height of around three to four meters above ground (Table 1). We sampled at multiple heights per tor, starting below the soil surface of each tor in order to assess exhumation through time. On average, five 2 kg samples of rock, or 0.5 kg of quartz vein material, were sampled within the uppermost 1–3 cm of the rock surfaces using an electric stone saw or chisel and hammer (Table 1). Each sampling site was recorded by GPS (global positioning system) and verified with topographic maps. The individual geometry of each tor and its topographic shielding, dip and dip-direction of the rock surface were recorded.

3.3. Laboratory procedure for surface exposure dating (¹⁰Be)

All rock samples were individually crushed and about 0.4 kg of the 0.6–0.25 mm fraction was retained. The material was then processed according to standard practice (Kohl and Nishiizumi, 1992), which is now summarised. The retained fraction was treated with *aqua regia* (1:4.22 of 65% HNO₃ to 32% HCL) for up to 36 h to eliminate iron oxides, organic material and carbonates. The remaining mineral assemblage underwent a 1 h treatment with 0.4% HF. A flotation system after Kitchener (1984) was used to physically separate mica and feldspar from quartz. Remaining contaminants were removed with 4% HF leaching cycles (7–21 days). The resulting 20–30 g of pure quartz was spiked with a ⁹Be-carrier solution (Scharlau, BE03460100) and together dissolved in 40% HF. We isolated Be using anion and cation exchange columns followed by selective pH precipitation (von Blanckenburg et al., 1996). The Be (OH)₂ was calcinated to BeO for 2 h at 850 °C and mixed with Nb powder before pressing it into Cu-targets. The ETH Laboratory of Ion Beam Physics Accelerator Mass Spectrometry (AMS) facility measured the targets (0.5MV Tandy). The ¹⁰Be standard S2007N was used with a nominal ¹⁰Be/⁹Be value of 28.1×10^{-12} (Kubik and Christl, 2010; Christl et al., 2013). Standard S2007N was calibrated relative to the Nishiizumi standard ICN01-5-1 with a revised nominal value of 2.709×10^{-11} (Nishiizumi et al., 2007). The 1 σ error of S2007N is 2.7% (Christl et al., 2013). The measured ¹⁰Be/⁹Be ratios were corrected for the ¹⁰Be contribution of the Be-carrier (¹⁰Be/⁹Be blank ratio, $3.00 \pm 0.87 \times 10^{-15}$). Exposure ages were calculated using the cosmogenic nuclide online calculator v2.3 (Balco et al., 2008). The program uses a ¹⁰Be half-life of 1.387 ± 0.0012 Ma (Chmeleff et al., 2010; Korschinek et al., 2010) and a sea level high latitude ¹⁰Be production rate of 4.01 [¹⁰Be-atoms gram SiO₂⁻¹ year⁻¹] (Borchers et al., 2016; Putnam et al., 2010). The production rate was corrected for latitude and altitude after the scaling scheme of Stone (2000) and further corrected for the sample thickness according to the depth profile of Brown et al. (1992) with an effective radiation attenuation length of 160 g cm⁻² of Gosse and Philips (2001) and a constant rock density of 2.65 g cm⁻³ (Hatherton and Leopard, 1964). A variety of rock surface erosion rates were tested and no correction for snow was applied (Table 2). Related effects of geomagnetic field variations on the ¹⁰Be ages can be assumed to be negligible (Masarik et al., 2001; Pigati and Lifton, 2004).

3.4. Determination of surface denudation using ¹⁰Be

We calculated surface ages on the basis of rock surface erosion rates in the range of 0–2 [mm kyr⁻¹] (Table 2), to account for high surface abrasion (e.g. wind erosion) by a wide range of model exhumation values (heights versus age). Exhumation models were based on the best regression fits. We used polynomial (3rd order) functions as well as the logistic function (3) after Lichter (1998) to quantify the potential D_{Surface} ranges, and not just a single rate as is the case with linear function

Table 1
Sample characteristics of the investigated profiles along rock tors at three different geomorphic settings.

Samples series	Coordinates [WGS84]		Groundelevation [m a.s.l. ^a]	Sample material [–]	Sample thickness [cm]	Height above ground [cm]	Dip direction of rock surface [deg ^b]	Dip angle of rock surface [deg ^b]	Shielding factor [–]	Axis [–]
	Latitude	Longitude								
	[°S]	[°E]								
Location 1 (valley)										
Tor 1										
To1–1-Top	45°27.166′	170°20.687′	378	Schist	3	1130	28	15	0.998	z
To1–2-Middle	45°27.166′	170°20.687′	378	Schist	3	680	28	30	0.952	x
To1–3-Bottom	45°27.166′	170°20.687′	378	Schist	3	40	41	40	0.874	x
To1–4-Subsurface	45°27.166′	170°20.687′	378	Schist	4	–30	43	45	0.840	x
Tor 2										
To2–1-Top	45°28.166′	170°19.216′	384	Schist	3	400	290	5	1.000	z
To2–2-Middle	45°28.166′	170°19.216′	384	Schist	5	300	334	5	0.988	z
To2–3-Bottom	45°28.166′	170°19.216′	384	Schist	4.5	25	270	82	0.418	x
To2–4-Subsurface	45°28.166′	170°19.216′	384	Schist	3	–55	330	11	0.528	x
Tor 3										
To3–1-Top	45°28.591′	170°19.174′	404	Schist	3	420	320	16	0.997	z
To3–2-Middle	45°28.591′	170°19.174′	404	Qtz vein	4.5	205	160	45	0.920	y
To3–3-Bottom	45°28.591′	170°19.174′	404	Schist	7	55	140	75	0.641	y
To3–4-Subsurface	45°28.591′	170°19.174′	404	Schist	2.5	–45	146	75	0.627	y
Location 2 (Ridge)										
Tor 4										
To4–1-Top	45°29.873′	170°16.425′	581	Schist	2.5	524	282	7	1.000	z
To4–2-Upper	45°29.873′	170°16.425′	581	Schist	9	404	254	70	0.724	x
Middle										
To4–3-Middle	45°29.873′	170°16.425′	581	Schist	2.5	233	200	55	0.825	x
To4–4-Lower	45°29.873′	170°16.425′	581	Schist	8	110	216	50	0.854	x
Middle										
To4–5-Bottom	45°29.873′	170°16.425′	581	Schist	4.5	70	246	60	0.793	x
To4–6-Subsurface	45°29.873′	170°16.425′	581	Schist	4.5	–30	334	5	0.863	z
Tor 5										
To5–1-Top	45°29.652′	170°16.318′	541	Schist	9	380	189	52	0.877	z
To5–2-Upper	45°29.652′	170°16.318′	541	Qtz vein	5	275	187	81	0.529	x
Middle										
To5–3-Lower	45°29.652′	170°16.318′	541	Schist	2.5	195	15	88	0.502	x
Middle										
To5–4-Bottom	45°29.652′	170°16.318′	541	Schist	2.5	60	14	84	0.531	x
To5–5-Subsurface	45°29.652′	170°16.318′	541	Schist	3	–40	182	12	0.557	z
Tor 6										
To6–1-Top	45°29.158′	170°15.550′	435	Schist	3.5	515	358	10	0.999	z
To6–2-Upper	45°29.158′	170°15.550′	435	Schist	6	295	126	82	0.483	x
Middle										
To6–3-Lower	45°29.158′	170°15.550′	435	Schist	8.5	150	204	84	0.290	y
Middle										
To6–4-Bottom	45°29.158′	170°15.550′	435	Schist	4.5	80	125	90	0.445	x
To6–5-Subsurface	45°29.158′	170°15.550′	435	Schist	2.5	–25	123	85	0.455	x
Tor 7										
To7–1-Top	45°28.933′	170°15.524′	423	Schist	2.5	300	292	10	0.999	y
To7–2-Middle	45°28.933′	170°15.524′	423	Schist	9.5	130	160	85	0.481	y
To7–3-Bottom	45°28.933′	170°15.524′	423	Schist	4.5	20	140	85	0.446	y
To7–4-Subsurface	45°28.933′	170°15.524′	423	Schist	3	–30	346	4	0.446	z
Location 3 (off-site)										
Tor 8										
To8–1-Top	45°38.022′	170°11.802′	296	Schist	3	890	254	5	1.000	z
To8–2-Top2	45°38.022′	170°11.802′	296	Schist	2	755	60	85	0.558	x
To8–3-Upper	45°38.022′	170°11.802′	296	Qtz vein	4	435	78	80	0.611	x
Middle										
To8–4-Middle	45°38.022′	170°11.802′	296	Qtz vein	2.5	320	64	90	0.498	x
To8–5-Lower	45°38.022′	170°11.802′	296	Qtz vein	3	165	48	35	0.895	z
Middle										
To8–6-Bottom	45°38.022′	170°11.802′	296	Schist	3.5	25	38	30	0.894	z
To8–7-Bottom2	45°38.022′	170°11.802′	296	Qtz vein	3.5	10	350	70	0.527	y
To8–8-Subsurface	45°38.022′	170°11.802′	296	Schist	3	–10	38	15	0.971	z

^a Meters above sea level.

^b Degrees.

$$f(t) = \frac{a}{(1 + e^{b(t-c)})} + d \quad (3)$$

where $f(t)$ = height m (lowered surface), as a function of time, a = range of height [m], t = time years, b = slope coefficient –, c = time of the maximal rate of change years and d = asymptotic value m. Yet, these two functions include opposite preconditions. The classical polynomial function assumes a continuous surface denudation

prior to and after the time span covered by the surface exposure ages of the investigated tor. In contrast, the logistic function excludes these times and fits surface denudation rates for the measured time span only. Thus, the integral of these functions is comparable for the time span of the calculated ages (i.e. sample height to age ratio is identical) yet their functions differ in the point in time of their maxima.

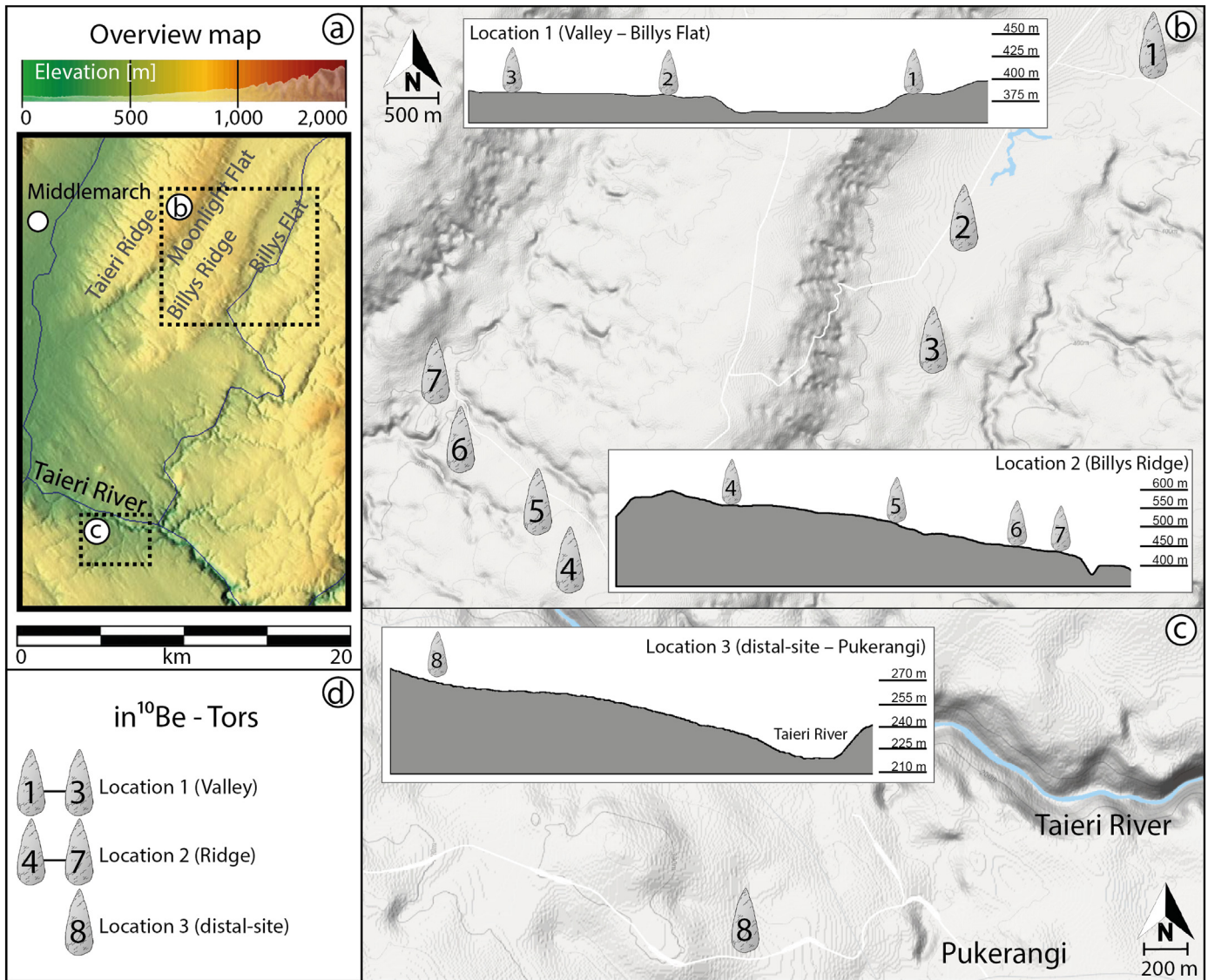


Fig. 2. The sample locations. (a) The sampling area showing key geographic locations including the local township of Middlemarch. The Background image is a digital elevation model coloured by elevation. (b) Position of sampled tors at the sampling locations “Valley” (Tor 1–3) and “Ridge” (Tor 4–7) (c) Position of Tor 8 at the “Distal” location. (d) The legend. Note, roads are depicted as white lines and rivers are blue lines in panels (b) and (c). The sample To6–5–Subsurface has been excluded in (a), (b) and (c). The digital elevation model was originally created by Geographx (geographx.co.nz) and was primarily derived from January 2012 LINZ Topo50 20 m contours ([data.linz.govt.nz/layer/768](https://data.linz.govt.nz/layer/51768-nz-8m-digital-elevation-model-2012)) and sourced here: <https://data.linz.govt.nz/layer/51768-nz-8m-digital-elevation-model-2012>.

The height-age relation of the exhuming tors was modelled by taking the error ranges of the ^{10}Be measurements into account, using Monte Carlo simulations and the previously noted regression fits. We used the mathematical derivative of these functions to determine the exposure and, thus, D_{Surface} . When applicable, we accounted for the age of the rocks' initial surface exposure (subsurface ^{10}Be accumulation; t_s), following Raab et al., 2018:

$$\frac{\partial f_{(t-t_s)}}{\partial t} = D_{\text{Surface}} \quad (4)$$

Unnatural exposure trends (youngest exposure age on the tor top, oldest at its base) were not modelled (e.g. Tor 6) due to the wide range of assumptions (i.e. inversion, undercutting, irregular breakoffs). Age profiles with clear outliers (e.g. exceptionally young ages in comparison to the neighbouring samples) resulted in alternative models being selected that excluded outliers (e.g. ALT-MODELS, Tor 2).

4. Results

4.1. Schist tor ^{10}Be content

We investigated eight tors with 38 successful measurements (Table 2). Two samples (To1–4 & To2–1) could not be measured due to Be loss during chemistry and insufficient material for an additional extraction. The measured in situ ^{10}Be contents range from 10.37 to 191.56×10^4 [atoms g^{-1}] with an average of 44.8×10^4 [atoms g^{-1}]. The content errors span from 2.2% to 11.8% (Table 2). In general, the ^{10}Be content increases with tor height (Fig. 3a), but the highest content was measured at sample Tor 6–5 below the soil surface. Tor 1 in the valley and Tor 8 at the distal location share similar increasing content trends with height above ground, in contrast to the other tors (Fig. 3a). Schist tor samples selected along the structural x- or z-axis generally resulted in higher contents relative to samples selected along the y-axis (Fig. 3b). The maximal ^{10}Be content of distal Tor 8

Table 2Calculated exposure ages (\pm uncertainty) based on ^{10}Be concentrations (\pm error) and different rock surface erosion rates ($E_0 = 0$ [mm kyr^{-1}], $E_1 = 1$ [mm kyr^{-1}], $E_2 = 2$ [mm kyr^{-1}]).

Samples series	^{10}Be		Height [m]	Calculated exposure ages of different rock surface erosion rates		
	Concentration	Error		E0	E1	E2
	[10^4 atoms g^{-1}]	[%]		[a]	[a]	[a]
Location 1 (valley)						
Tor 1						
To1-1-Top	67.64 \pm 2.46	3.64	11.30	121,888 \pm 10,933	136,273 \pm 13,780	156,471 \pm 18,615
To1-2-Middle	38.17 \pm 1.68	4.41	6.80	71,142 \pm 6552	75,687 \pm 7438	81,106 \pm 8598
To1-3-Bottom	13.80 \pm 0.80	5.78	0.40	27,672 \pm 2728	28,319 \pm 2859	29,009 \pm 3003
To1-4-Subsurface ^a	(-) \pm (-)	(-)	-0.30	(-) \pm (-)	(-) \pm (-)	(-) \pm (-)
Tor 2						
To2-1-Top ^a	(-) \pm (-)	(-)	4.00	(-) \pm (-)	(-) \pm (-)	(-) \pm (-)
To2-2-Middle	64.13 \pm 2.36	3.68	3.00	117,822 \pm 10,576	131,176 \pm 13,212	149,649 \pm 17,583
To2-3-Bottom	41.13 \pm 1.03	2.51	0.25	176,839 \pm 15,324	209,176 \pm 21,907	265,384 \pm 38,054
To2-4-Subsurface	22.71 \pm 0.80	3.53	-0.55	75,030 \pm 6615	80,053 \pm 7560	86,090 \pm 8816
Tor 3						
To3-1-Top	74.66 \pm 3.02	4.05	4.20	131,867 \pm 12,099	148,974 \pm 15,594	173,913 \pm 21,901
To3-2-Middle	71.01 \pm 2.79	3.92	2.05	137,606 \pm 12,564	156,376 \pm 16,403	184,334 \pm 23,582
To3-3-Bottom	39.98 \pm 1.89	4.74	0.55	111,917 \pm 10,603	123,757 \pm 13,065	139,736 \pm 16,999
To3-4-Subsurface	21.01 \pm 1.04	4.95	-0.45	57,188 \pm 5409	60,049 \pm 5977	63,326 \pm 6678
Location 2 (ridge)						
Tor 4						
To4-1-Top	97.85 \pm 4.72	4.83	5.24	147,715 \pm 14,193	169,779 \pm 18,981	204,133 \pm 28,598
To4-2-Upper Middle	84.75 \pm 3.14	3.71	4.04	186,979 \pm 17,106	224,518 \pm 25,207	294,870 \pm 47,564
To4-3-Middle	66.29 \pm 1.47	2.21	2.33	120,136 \pm 10,159	134,065 \pm 12,754	153,493 \pm 17,115
To4-4-Lower Middle	76.07 \pm 1.79	2.36	1.10	139,946 \pm 11,950	159,442 \pm 15,686	188,768 \pm 22,786
To4-5-Bottom	37.02 \pm 1.02	2.75	0.70	70,010 \pm 5959	74,401 \pm 6750	79,619 \pm 7781
To4-6-Subsurface	25.20 \pm 0.78	3.08	-0.30	43,557 \pm 3733	45,198 \pm 4025	47,016 \pm 4365
Tor 5						
To5-1-Top	59.44 \pm 2.59	4.36	3.80	110,320 \pm 10,233	121,887 \pm 12,578	137,471 \pm 16,305
To5-2-Upper Middle	55.36 \pm 1.54	2.78	2.75	165,493 \pm 14,449	193,614 \pm 20,124	240,470 \pm 32,977
To5-3-Lower Middle	35.93 \pm 1.21	3.37	1.95	109,266 \pm 9643	120,477 \pm 11,813	135,455 \pm 15,226
To5-4-Bottom	23.17 \pm 0.77	3.30	0.60	66,018 \pm 5747	69,871 \pm 6457	74,390 \pm 7365
To5-5-Subsurface	13.82 \pm 0.57	4.16	-0.40	37,457 \pm 3375	38,652 \pm 3598	39,953 \pm 3852
Tor 6						
To6-1-Top	74.78 \pm 8.84	11.82	5.15	128,689 \pm 18,897	144,906 \pm 24,182	168,265 \pm 33,536
To6-2-Upper Middle	61.24 \pm 2.05	3.35	2.95	224,107 \pm 20,345	280,993 \pm 33,137	413,827 \pm 86,492
To6-3-Lower Middle	57.88 \pm 2.20	3.80	1.50	364,794 \pm 35,077	565,775 \pm 97,029	0 ^b \pm 0 ^b
To6-4-Bottom	38.83 \pm 1.57	4.03	0.80	149,257 \pm 13,745	171,360 \pm 18,387	205,449 \pm 27,653
To6-5-Subsurface	191.56 \pm 6.17	3.22	-0.25	836,190 \pm 88,554	0 ^b \pm 0 ^b	0 ^b \pm 0 ^b
Tor 7						
To7-1-Top	11.49 \pm 0.64	5.60	3.00	19,292 \pm 1877	19,604 \pm 1939	19,930 \pm 2005
To7-2-Middle	35.98 \pm 1.50	4.18	1.30	134,330 \pm 12,415	151,835 \pm 16,051	177,312 \pm 22,640
To7-3-Bottom	24.40 \pm 1.28	5.26	0.20	93,265 \pm 9059	101,193 \pm 10,730	111,233 \pm 13,145
To7-4-Subsurface	17.83 \pm 1.19	6.65	-0.30	66,894 \pm 7025	70,826 \pm 7903	75,443 \pm 9028
Location 3 (off-site)						
Tor 8						
To8-1-Top	44.17 \pm 1.12	2.55	8.90	84,470 \pm 7161	90,998 \pm 8345	99,093 \pm 9994
To8-2-Top2	30.06 \pm 0.92	3.06	7.55	101,370 \pm 8808	110,890 \pm 10,611	123,273 \pm 13,330
To8-3-Upper Middle	21.00 \pm 0.92	4.38	4.35	65,295 \pm 5996	69,055 \pm 6727	73,456 \pm 7659
To8-4-Middle	13.68 \pm 0.63	4.59	3.20	51,080 \pm 4728	53,326 \pm 5165	55,855 \pm 5689
To8-5-Lower Middle	10.37 \pm 0.69	6.63	1.65	21,769 \pm 2258	22,166 \pm 2342	22,583 \pm 2433
To8-6-Bottom	10.79 \pm 0.76	7.00	0.25	22,785 \pm 2419	23,221 \pm 2513	23,680 \pm 2616
To8-7-Bottom2	10.61 \pm 0.47	4.40	0.10	37,693 \pm 3441	38,896 \pm 3669	40,207 \pm 3930
To8-8-Subsurface	19.73 \pm 0.92	4.69	-0.10	38,390 \pm 3560	39,655 \pm 3803	41,037 \pm 4080

Note: Calculation was performed using the cosmogenic nuclide online calculator v2.3 (Balco et al., 2008) and the scaling scheme of Stone (2000).

^a Sample could not be measured due to loss of ^{10}Be during target chemistry.^b Sample is oversaturated under this rock surface erosion rates.

(~300 m a.s.l.) was only half of the content of the tors at the valley (~430 m a.s.l.) and ridge (~550 m a.s.l.) locations, where the highest ^{10}Be contents (Fig. 3c) were measured. Content below $\sim 25 \times 10^4$ [atom g^{-1}] are primarily found in the subsurface samples (Fig. 3d). The subsurface samples range from 13.82 to 25.20×10^4 [atom g^{-1}], averaging 20.1×10^4 [atom g^{-1}] and having an error range of 3.1% to 6.7% (Table 2), with the exception of sample Tor 6-5-Subsurface (191.56×10^4 [atom g^{-1}], 3.2% error; Table 2; Fig. 3d).

4.2. Schist tor surface exposure ages

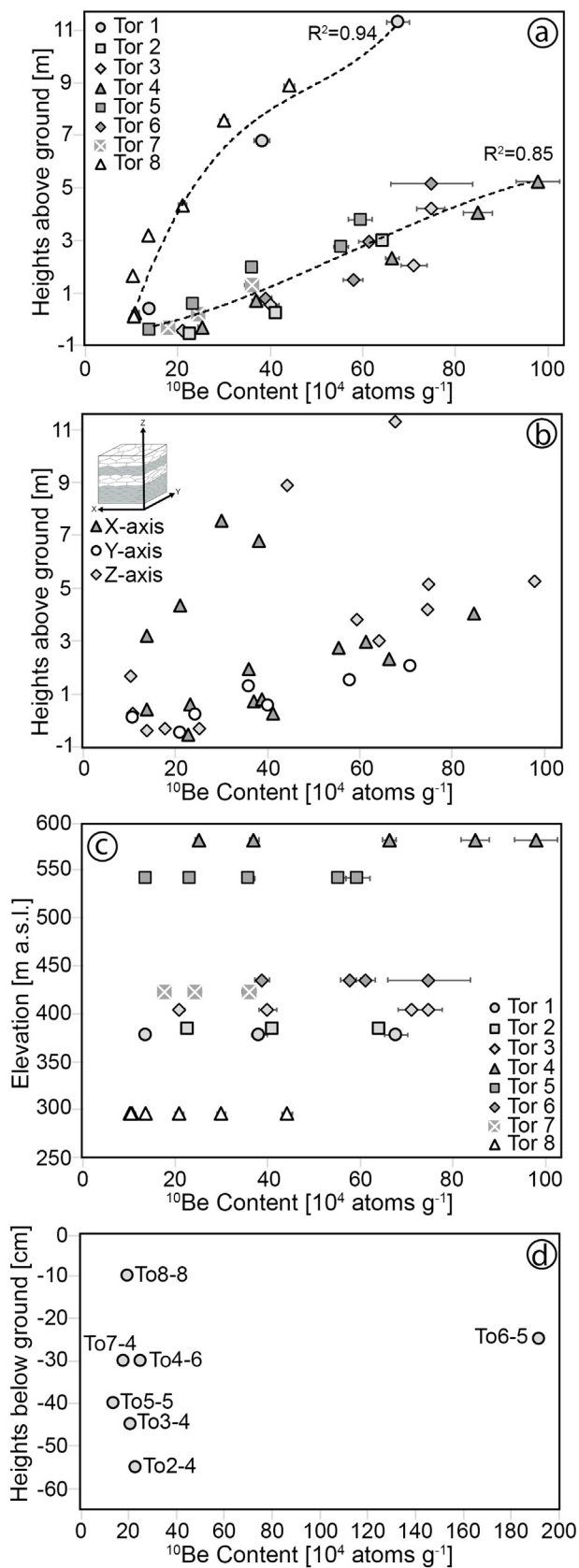
Calculated exposure ages (\pm uncertainty) average around 122 ± 12 ka and range from 836 ± 89 ka to 19 ± 2 ka depending on rock surface

erosion rates (Table 2). The vertical age trends along the schist tor surfaces (Fig. 4a-h) reflect the ^{10}Be content trends (Fig. 4a). Most of the tors display age-height patterns with one or more inconsistent ages. Larger inconsistencies along the vertical profile series are found in Tor 2, 5, 6 and 7 (Fig. 4b,e,f,g). The small age discrepancies in Tor 4 and 8 (Fig. 4d,h) are within error ranges of adjacent samples. The reversal age of 194 ± 20 ka at Tor 5 was a quartz-vein (Table 2). Only Tor 1 and 3 (Fig. 4a,c) did not reveal age inversions.

4.3. Modelled surface denudation rates

Based on the successful schist tor ^{10}Be measurements and calculated exposure ages, and our previous experience with modelled surface

denudation rates in granitoid terranes, we are confident that modelled surface denudation rates can be calculated from Otago schist rocks. In the simplest terms, tor-based denudation rates are the ratio of sampling



heights above ground and surface ages, with the basic assumption that the oldest surface ages are at the top of the tor. This is clearly not the case for Tor 6 (Fig. 4f), and thus was excluded from modelling. All other tors showed an overarching increasing age trend from bottom to top that allowed modelling within the surface exposure age variations. Assuming that the landscape has lowered continuously, the measured surface age variations with magnitudes of more than 10^4 years within a few meters of tor height, are likely the result of changes in shielding and erosion. These abrupt and unreconstructable changes result in age inversion along the profiles by resetting the terrestrial cosmogenic nuclide signature at the rock surface. We interpret that only half of the investigated tors have had a rather undisturbed surface exposure history (Tor 1, 3, 7, 8). Tor formation is more irregular at the ridge location relative to the valley, compared to only one out of three tors at the valley, yet all four tors at the ridge, experienced some form of surface rejuvenation.

In detail, four tors (Tor 2, Tor 4, Tor 5, Tor 7) had single ages deviating from the vertically increasing age trend, complicating the modelling approach. The sample To2-2 and To2-3 are 60 ka years apart. Since the To2-1 was unmeasurable, the age continuation towards the top is unknown. However, To2-4 reached the highest subsurface sample age (excluding Tor 6). Thus, one would also expect older surface ages at the top, relative to other tors. We suggest that the surface of To2-2 has undergone either a rejuvenation process (e.g. break-off) or was heavily shielded (e.g. by a tafoni roof). We provide three models to account for these scenarios (Fig. 5c,d). The surface age differences of To4-1 to To4-2 and To4-3 to To4-4 are minor since the ages overlap partially (Fig. 6a). The overarching age trend is clear due to the number of samples. Thus, we consider that To4-1 and To4-3 have undergone similar processes as To2-2. In contrast, the significantly older surface age of To5-2 is potentially the result of sampling a quartz vein, which is more resistant to surface erosion compared to schist. Yet, a rejuvenation of the tor top (To5-1) cannot be excluded, resulting in two modelling options. The sample To7-1 is clearly identified as an outlier due to a rock break-off, given its young age (~23 ka).

Given the discussion above, the age profiles along schist tors are more challenging for modelling than magmatic tors. However, schist tor modelling is still feasible with careful pre-selection of modelling points, as is done here. A variety of models were applied owing to the stated outliers and age inversions (e.g. Figs. 5c,d; 6a, h) which in summary show the D_{Surface} rates in the valley reach maxima of ~ 0.22 [m kyr^{-1}] (Tor 1; Fig. 5b), ~ 0.06 – 0.2 [m kyr^{-1}] (Tor 2; Fig. 5d) and ~ 0.15 [m kyr^{-1}] (Tor 3; Fig. 5f). Average values range from ~ 0.04 to ~ 0.15 [m kyr^{-1}]. At the ridge location, the D_{Surface} values differ among the applied models. Depending on the modelling approach, erosion maxima close to the ridge crest are about 0.03 [m kyr^{-1}] (Tor 4; Fig. 6b) or 0.04 – 0.08 [m kyr^{-1}] (Tor 5; Fig. 6d). Towards the foot of the slope the erosion maxima decrease to ~ 0.035 [m kyr^{-1}] (Tor 7; Fig. 6h). Overall, the modelled D_{Surface} rates at the valley appear to be two to six times higher than at the ridge. The distal location (Fig. 2c) also resulted in about ten-fold higher rates, with erosion maxima of up to 0.2 [m kyr^{-1}] (Tor 8; Fig. 7b), comparable to the valley rates, around 0.15 [m kyr^{-1}].

We consider that the valley has undergone a continuous surface lowering for about 160 ka (Tor 1; Fig. 4a) to about 170 ka (Tor 3; Fig. 4c). The somewhat contradictory age of ~ 210 ka in the middle of the valley (Tor 2; Fig. 4b), is most likely due to missing past shielding information (see Fig. 8b). The incision processes by wind, thalweg runs, rivers or creeks are plausible destabilising drivers at tor bases (Fig. 8).

Fig. 3. Plots of ^{10}Be versus various parameters. (a) Measured ^{10}Be concentrations as a function of height above ground (with related trend curves) of all samples. (b) Relation of ^{10}Be concentrations and sample position at the structural axes of the schist, where the x-axis is parallel to the dominant fabric (L- and S-fabric), the y-axis horizontally and the z-axis vertically-perpendicular to the dominant fabric of the schist. (c) The ^{10}Be concentrations in relation to elevation in meters above sea level (m a.s.l.). (d) The ^{10}Be concentration of subsurface samples. The sample To6-5-Subsurface has been excluded in (a), (b) and (c).

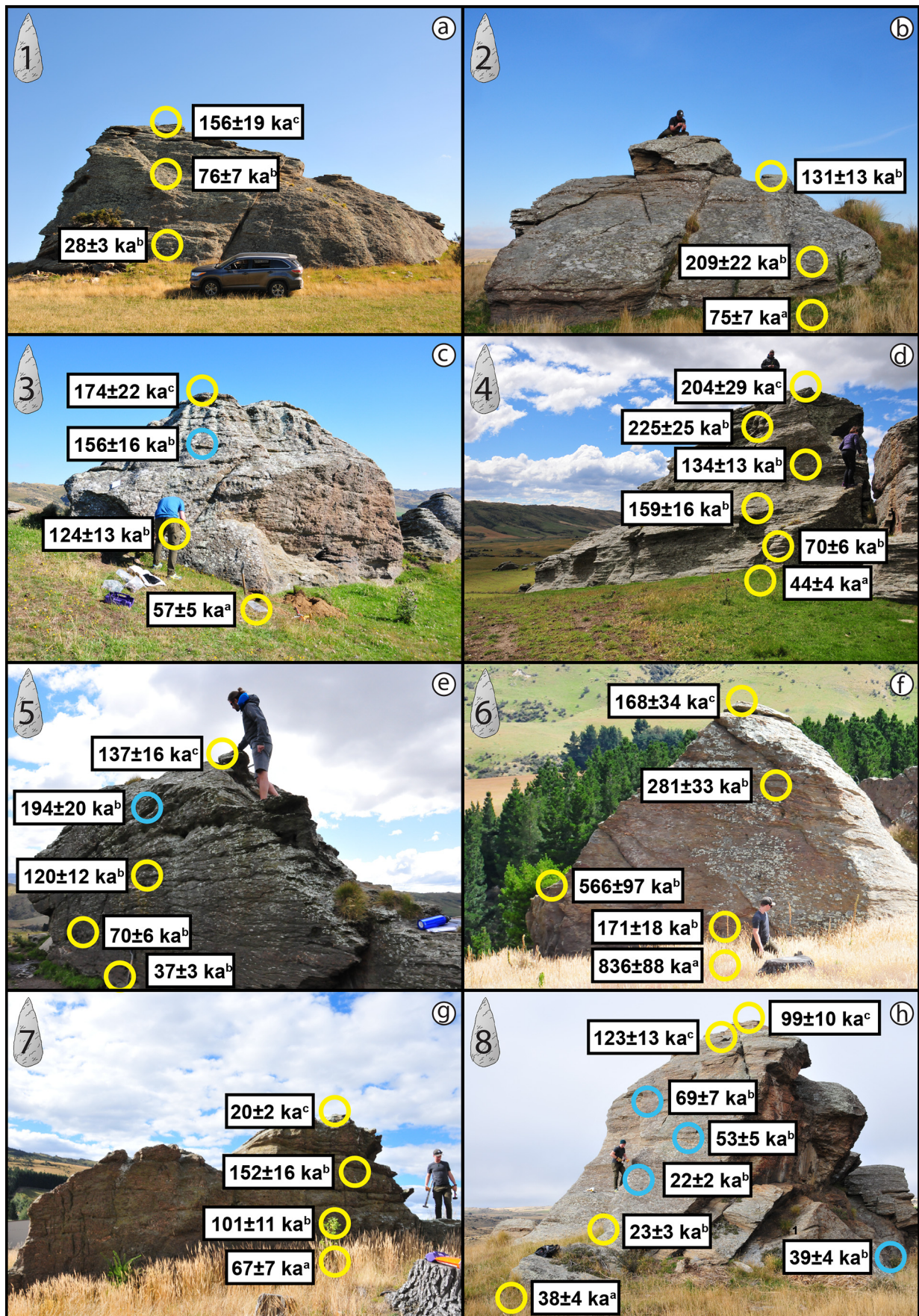


Fig. 4. Exposure ages (a–h) along the tor profiles (Table 2; exposure ages of different rock surface erosion rates $ka^a = E_0 = 0$ [mm kyr^{-1}], $ka^b = E_1 = 1$ [mm kyr^{-1}], $ka^c = E_2 = 2$ [$\text{s[mm kyr}^{-1}]$]). The circles indicate the sampling position along the tor. Yellow circles are used for schist samples, blue circles for quartz veins.

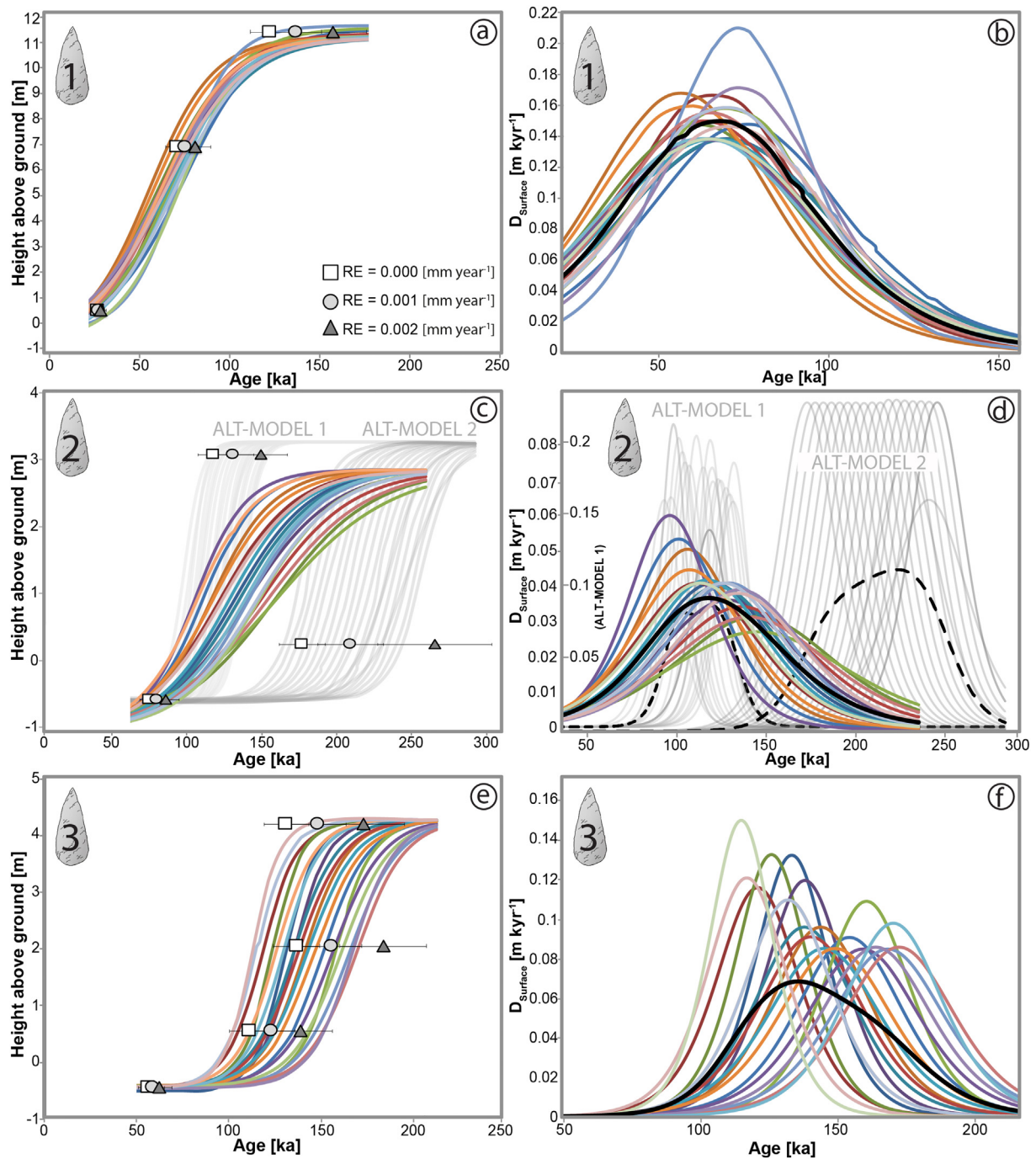


Fig. 5. Exposure ages as a function of tor height and derived surface denudation rates ($D_{Surface}$) based on Monte Carlo simulations for Tor #1 (a, b), Tor #2 (c, d) and Tor #3 (e, f) at Location 1. Dark lines (b, d, f) reflect model averages. The grey lines represent alternative models (ALT-MODEL 1, 2) and dashed black lines represent the model averages (d). RE = rock erosion. (For interpretation of the references to colour in this figure, the reader is referred to the web version of this article.)

Subsurface ages determined in this study overlap with the age range assigned to proximal alluvial fans at about ~30 ka (Nicolls, 2020). Samples taken at similar altitudes, for example To1–2–Middle at ~385 m a.s.l. and the To2–4–Subsurface at ~382 m a.s.l., have overlapping ages of ~75 ka. Overlapping ages at the Billys Flat site between To1–1–Top at ~389 m a.s.l. and To3–2–Middle at 406 m a.s.l. ~160 ka (Table 2, Fig. 4a,c) support the general timing of the valley formation.

Assuming that surfaces at ~380 m a.s.l and ~400 m a.s.l have been exhumed at about 75 ka and 160 ka respectively, a lowering rate of 0.24 [m kyr⁻¹] can be calculated. This rate would represent the average surface lowering of the entire valley. The Monte Carlo averages of the valley location (Fig. 5) indicate higher surface lowering rates peaked around 75

ka and 150 ka. In detail, Tor 1 peaks at ~1.7 [m kyr⁻¹], ALT-MODEL 1 of Tor 2 also peaks at ~1.7 [m kyr⁻¹] and Tor 3 at ~1.2 [m kyr⁻¹]. These modelled peaks might be related to certain events during tor exposure that are the result of, for example, wind erosion, river incision, tafoni formation or rock chipping.

5. Discussion

5.1. Schist tor and Otago landscape surface ages

Fahey (1981) suggested the majority of Otago tors are polygenetic and formed as a response to diverse weathering agents operating at

different times through the Pleistocene. Our investigated tor surfaces exhibit an oldest age of over 800 ka, an average age at around 122 ± 12 ka and youngest ages of less than 20 ka. The youngest ages correlate well with the results of Kim and Englert (2004) who calculated in situ ^{10}Be erosional ages of 36–22 ka for the Otago Schist (quartz taken from quartz veins at the Macraes Gold Mine, East Otago). Additionally, surface exposure erosional ages of Jackson et al. (2002) range from ~66 ka to ~44 ka for the Otago Schist and about 800–85 ka for sarsen stones that are relicts weathered from overlying strata. A study of quartz-rich boulders by Bennett et al. (2006) yielded surface erosional age ranges of over ~1000 ka to ~100 ka at elevations from 780 to 530 m a.s.l. The ^{10}Be erosional ages on sarsen stones by Youngson et al. (2005) also range from ~1300 to ~400 ka for North Rough Ridge, and 550–90 ka for South Rough Ridge, with both locations being c. 40 km northwest of Billys Flat.

Inland Otago sedimentary river terrace depositional ages are in general about 60–20 ka, while various alluvial fans range in age between ~650–450 ka, ~250–60 ka and ~150–20 ka depending on their location (Craw, 2013). Along the east coast of Otago, deposited sand of the Taieri Beach (south of Dunedin) yielded depositional ages of 117 ± 13 ka (optical dating, K-feldspar) and 117 ± 12 ka (TL dating, quartz; Litchfield and Lian, 2004). These ages fit well with our average tor surface ages of 122 ± 12 ka. Yet, earlier studies by Rees-Jones et al. (2000) calculated quite younger depositional ages for loess (19 ± 7 & 22 ± 7 ka), dune sand (47 ± 15 ka) and beach sand (71 ± 14 ka) at Taieri Beach with optically stimulated luminescence (OSL). The ages of the coast, river terrace and alluvial fan deposits overlap with the age range of the investigated tors at all sites in this study. Adjacent to our research area, Moonlight Flat (Fig. 2a) lacustrine deposit (without any other evidence for Pleistocene lakes) samples also studied by OSL, recently yielded an age at about 12.9 ± 1.1 ka, together with mud lenses within fluvial gravel (~10 ka) and loess above fluvial gravels (~7 ka; Nicolls, 2020). These ages are seen as the minimum surface age. The overlap in tor exposure ages and erosional/depositional ages determined across lowland and coastal areas in Otago suggests a possible meaningful relationship between the two settings that is discussed in Section 5.4.

5.2. Schist tor formation patterns

Based on the partially inconsistent age profiles, we propose four main tor formation patterns (Fig. 8), however, individual tors can also exhibit a mix of the following processes. A simple continuous tor exposure process starts with selective weathering along joints which are mostly sub-vertical in the study area (e.g. Stirling, 1991). The weathering mantle forms around a core stone that has an inherent structure. The tor age profiles suggest that the saprolite must have been removed rather quickly (~0.15 [m kyr⁻¹]) by aeolian or fluvial erosion. Afterwards low-land tors primarily experience equally distributed rock erosion without tafoni structure formation. The continuous exposure results in a straight-forward increasing ^{10}Be trend from the base towards the top.

The “mushroom-like” exposure is characteristic for sarsen stones in Otago (Youngson et al., 2005). We suggest that this process is also found in schist tors. During saprolite formation the base of the present-day tor has been weakened. Subsequently, after the weathering mantle has been removed, the base becomes more prone to erosion (fluvial or aeolian) hollowing the bottom of the tor (or the tor position facilitates base incisions). The undercutting progresses until a point of failure of the overhanging roof has been reached. The break-off material shields the bottom surface against erosion and yet continues to enable further production of TCN. Subsequent breakoffs restarted this cycle, until the collapse of the above structure. Due to this bottom-up disintegration of the tor, highest ^{10}Be content is expected at the bottom and not at the top of the tor.

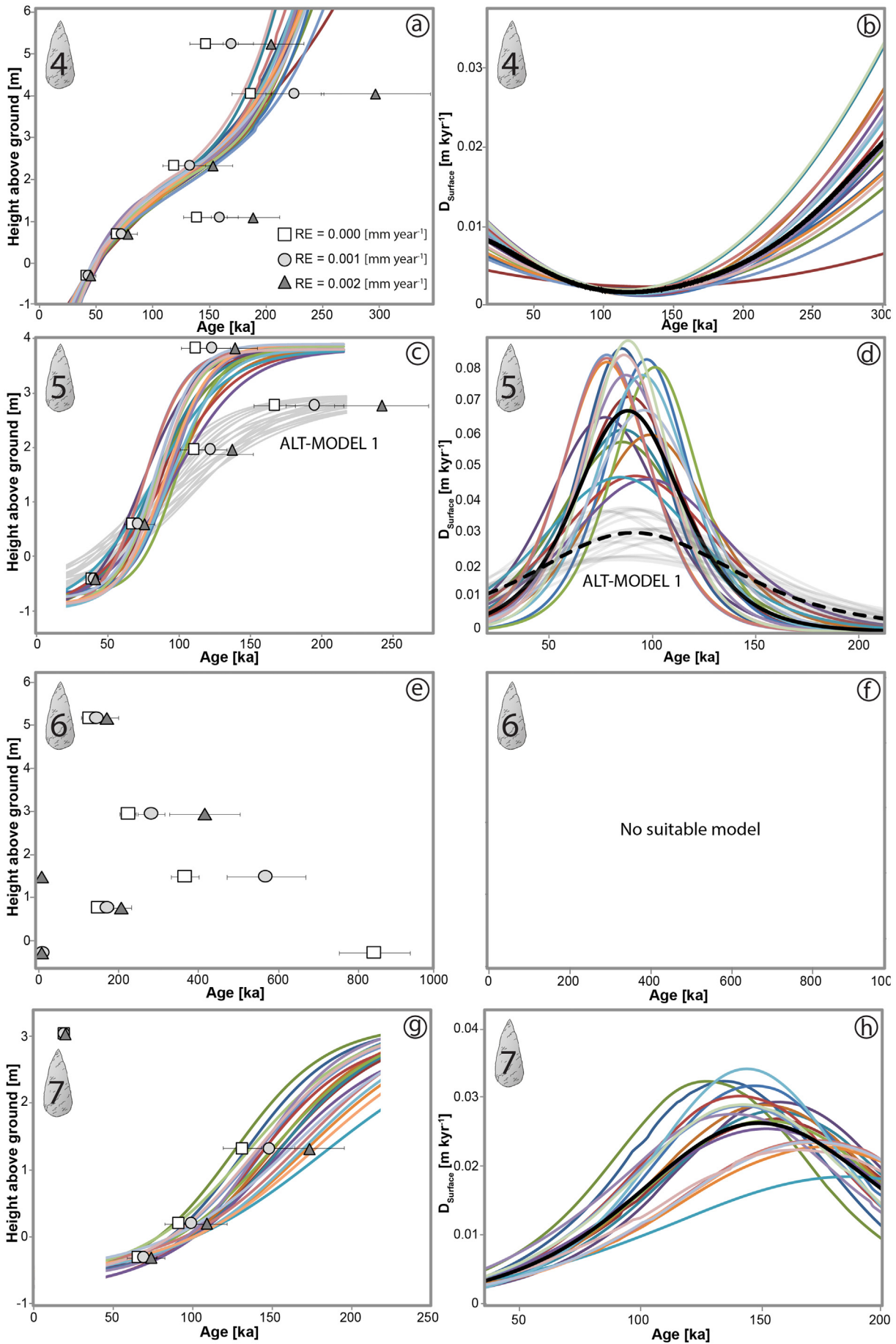
Additionally, multiple tafonis can form over time. Once the tor starts surfacing, wind erosion can commence hollowing the surface, which

progresses with further exposure of the tor. The hollowing of the tor increases the attenuation depth of cosmic rays, and thus increases ^{10}Be production of an inner rock surface. The tafoni structures weaken the stability of the tor until parts of it collapse. In contrast to the mushroom-like exposure, the collapsed material can remain on the tor (see collapse picture in Fig. 8), and partially shield the bedrock from further aeolian erosion and cosmic rays. Surfaces of tafoni shaped tors do not follow classical production rates of cosmogenic nuclides. Thus, surface ages can vary irregularly with height. We consider this process to be the most dominant process in Otago since most tors at our investigated area are found to be hollowed out, some with human-sized cave-like structures. Following Raeside (1949) and Youngson et al. (2005), we suggest that wind erosion has strongly influenced the form and shape of schist tors of Otago.

The final process relates to the structurally steep to sub-vertical joint planes of the tors occurring at high angles to the sub-horizontal (average 0–5 degrees) dip-angle of the schistosity (Martin et al., 2016a,b; Weinberger et al., 2010; Brown, 1968). This intersection between different fabric sets at different orientations is often a weakness zone where one or more failure planes can occur. Such failures are the result of preferential circulation of water, controlled by the schistose fabric, that may lead to the formation of clays. Clay formation changes the geomechanical properties of the parent rock and reduces its initial strength (Calcaterra and Parise, 2010). The later removal of surrounding weathered rock (saprolite) during ongoing tor exposure can remove the physical support of a part of the tor, causing the sliding of rock plates or blocks along the failure plane (Fig. 8). Thus, such process would result in a local surface exposure rejuvenation.

We attribute the following process to our investigated tors, based on their surface exposure ages and general appearance in field. The three surface ages of Tor 1 indicate a continuous surface exposure history from bottom to top (Fig. 5a) resulting in clear modelling paths and denudation rates of 0.02–0.2 [m kyr⁻¹]. Furthermore Tor 1 lacks tafoni structures and no apparent breakoff along joint planes has been observed (Fig. 4a). In contrast, the top two surface ages of Tor 2 are inverted (Fig. 5c). Observed in the field and shown in Fig. 4b, remnants of tafoni structures and cracks along plates parallel to the schistosity indicate prior hollowing out by wind erosion, which could have led to the younger age of To2–2. For example, Tor 2 at ~200 ka could have formed a roof from wind erosion, resulting in the higher ages at the bottom of the tor. Possibly, that roof then broke off at ~130 ka resulting in the 70 ka younger age at To2–2-Middle. We considered three scenarios for Tor 2 during the modelling resulting in different D_{Surface} rates. ALT-MODEL 1 (Fig. 5c,d) considers To2–3 to as outlier resulting in similar rates to Tor 1. The ALT-MODEL-2 excludes To2–2 as outlier having lower D_{Surface} rates (0.08–0.01 [m kyr⁻¹]). The coloured lined model of Tor 2 is an average model (range of 0.15–0 [m kyr⁻¹]), that considers the buffering of tor disintegration by the shielding of collapse material that potentially once rested on the tor. Tor 3 has a similar straight-forward exposure age trend as Tor 1 (Fig. 5e), resulting in comparable D_{Surface} rates (Fig. 5f). In the field we have seen a clear and fresh face along a joint plane (Fig. 4c), yet no break-off rock material was found in proximity (though human removal during farming practices may have occurred). The clear surface age trend points towards a continuous exposure process, yet the fresh and planar face means a structural component cannot be ruled out.

The tors along the ridge segment are dominated by tafoni exposure processes. The steep sampled surface of Tor 4 is scattered with tafoni like incisions. Break-offs or sliding events might have occurred at about 200 ka and a second event at ~130 ka (Fig. 4d). For our model (Fig. 6a, b) we have considered the surface age of To4–4 to be a result of an increased attenuation depth due to wind erosion. If the age of To4–3 would have been the result of a break off around 130 ka, then the model and thus D_{Surface} would be even lower (<0.05 [m kyr⁻¹]) from ~75–160 ka. The presented model (Fig. 6b) already depicts very low denudation rates during these times.



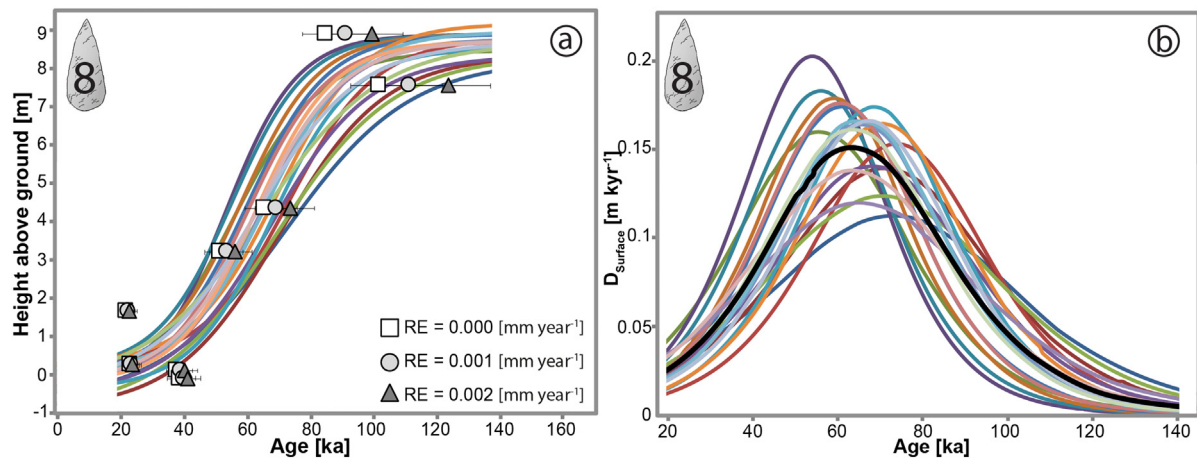


Fig. 7. Exposure ages as a function of (a) tor height and (b) derived surface denudation rates (D_{Surface}) based on Monte Carlo simulations for Tor #8 at Location 3. Dark line in (b) reflects the model average. RE = rock erosion.

Tor 5 was sampled along a planar face, potentially a former joint plane. Despite this, the surface exposure ages continuously increase from bottom to top, with only a mild resetting of the top surface age. It is difficult to assess if either To5–1 is an outlier created by rock removal, or To5–2 is an outlier due the higher erosion resistance of quartz. Therefore, we used each of the tor top ages for an individual model to provide a potential range of D_{Surface} rates, which can be compared to other tors. The fact that the peak of the ALT-MODEL 1 (Fig. 6d) matched the model of Tor 4 and Tor 7 of the ridge, points towards a rejuvenation process of the tor top (To5–1).

Tor 6 at the foot slope of the ridge (Fig. 2b) differs significantly in its timing to all other tors. The age inversion of Tor 6 (Fig. 6e) can be explained by continuous undercutting and breakoffs (Fig. 8) which we assign to a “mushroom-like” exposure process. The nearly planar face (Fig. 4f) might have been the primary break-off point. Therefore, we also consider that a former vertical joint has been a key component to this specific inversion process. Under these circumstances of multiple potential combinations of surface exposure, no reasonable model could be derived, but surface denudation rates must have been low given the high surface ages. Tor 7 with a clear outlier on top due to structural failure and a continuous vertical age profile enabled a simple surface denudation model for the last ~150 ka (Fig. 6g,h). The model agrees well with the other tors along the ridge.

Similar structural rejuvenations along steep (sliding) faces are found at distal Tor 8 (Fig. 4h). Since very young surface ages within a clear age trend are easily detected as outliers (e.g. To8–5, To8–6), modelling was achieved within the age variations of the remaining surface ages (Fig. 7a,b). Rejuvenation might have occurred at about 22 ka, which is over 10 ka younger than the surrounding surface samples with ages at ~38 ka (Fig. 4h). Thus, the distal location Tor 8 (Fig. 2c) has likely experienced a break-off because of sub-vertical joints (see field picture of joints in Fig. 8) while being otherwise continuously exhumed for ~120 ka (Fig. 4h). The resulting surface denudation rates of 0.05–0.2 [m kyr^{-1}] are in a comparable range to the valley tors. We note that Tor 1 (in the valley), Tor 4 (ridge) and Tor 8 (near Pukerangi) have similar surface exposure ages and maxima, despite being at different locations. Thus, any difference in the overall erosion rates appears to be lower than the resolution of this model. The peak phase at the distal site is around 70 ka, a similar time to the valley tors and Tor 5 at the ridge location. Also, the near- and sub-surface sample ages agree among all

locations (Tor 8, Tor 1, Tor 5 and Tor 4). Overall, tors at the ridge have slightly higher surface ages near, or at, the tor top compared to the valley tors.

In summary, exposure patterns appear to range from continuous exposure without (at least not captured) additional influences, mushroom exposure through tor base incision, tafoni formation which are more common at the exposed ridge location and structural failure through support (e.g. saprolite) removal (Fig. 8). Tors that underwent a partial self-protective process (e.g. mushroom, tafoni exposure), resulted in the oldest surface ages and lowest D_{Surface} rates (Fig. 8). We therefore see that schist tors form and decay at different rates depending on the underlying processes, and have a greater variation of exposure patterns compared to granitic tors (e.g. continuously exhumed, exfoliation processes; Migoñ, 2006).

5.3. Comparison of D_{Surface} to modern erosion (~60 years)

Erosion rates in Otago were determined using ^{137}Cs by Hewitt (1996) along a ridge near Earnsclough, Otago. Average erosion rates for crest and slopes (18° angle) were in the range of 0.42–1.02 [m kyr^{-1}]. The deposition rates at slope toes ranges between 0.05 and 0.09 [m kyr^{-1}] (Hewitt, 1996). Another ^{137}Cs investigation by Basher (2000), resulted in a similar range of ~0.6–1.1 [m kyr^{-1}] for backslopes and crests. These rates partly match, yet overall exceed the long-term D_{Surface} rates of this study.

Despite the gorge adjacent the Pukerangi site (Fig. 2c, Tor 8), the valley (Tor 1), the ridge (Tor 4) and distal locations (Tor 8) all show D_{Surface} rate erosion maxima of ~0.2 [m kyr^{-1}], that correlate with modern soil erosion rates. Yet, the fallout radionuclide-based erosion maxima of ~0.4–1.0 [m kyr^{-1}] by Hewitt (1996) are not found within the long-term rates of this study (e.g., Fig. 5). Thus, it seems that modern denudation rates (e.g. Hewitt, 1996; Basher, 2000) have increased by a factor of about ten at the ridge, while in the valley they increased just by a factor of about two to five, compared to our presented long-term D_{Surface} . We note that the fallout radionuclide derived rates only cover a time span of ~60 years, in contrast to the time span recorded by tors. Also, the caesium studies have targeted slopes and crests, which are generally prone to higher erosion compared to toe slopes, for example. We interpret that tors reveal an overall smoothed (and thus filtered) long-term erosion rate. Difference of long-term (e.g. $^{10}\text{Beryllium}$) and short-term

Fig. 6. Exposure ages as a function of tor height and derived surface denudation rates (D_{Surface}) based on Monte Carlo simulations for Tor #4 (a, b), Tor #5 (c, d), Tor #6 (e, f) and Tor #7 (g, h) at Location 2. The dark lines (b, d, h) reflect model averages. The grey lines represent alternative models (ALT-MODEL 1) and the model average is drawn as a dashed black line (d). The age inversion of Tor #6 did not allow a reasonable model solution. RE = rock erosion.

(e.g. fallout radionuclide) surface denudation rates has been detected by precious studies (e.g. Zollinger et al., 2015; Portes et al., 2018; Raab et al., 2018). Short-term erosion peaks (which may encompass the last ~60 years) are difficult to discern. However, during the last few decades, erosion rates distinctly increased due to human impact (Basher, 2010). The ecology of New Zealand changed drastically with the first European settlements (West, 2017; McGlone, 1983), in particular with respect to the introduction of ungulates and new farming practices (McWethy et al., 2009; Roche, 1994). Although the anthropogenic influence on soil erosion seems to play a decisive role, the exact relation to our study area cannot be determined.

5.4. Climate and surface denudation link

Erosion and subsequent denudation are strongly driven by climate. During warm and humid periods, higher $D_{surface}$ rates are often observed (e.g. Peizhen et al., 2001). These climate conditions are in general more prone to higher run-off and chemical weathering that produces more mobile material, which increases denudation and tor exposure rates. We compared tor surface ages and average $D_{surface}$ rates to warm period marine isotope stages (MIS; Lisiecki and Raymo, 2005).

The majority of tors in this study were exhumed between ~150 and ~50 ka, which overlaps MIS 5 between 130 and 71 ka. At the ridge, Tor 5 reflects the exposure and time pattern of Tor 1 and Tor 2 in the valley, and these overlap with MIS stages 6, 5 and 4. Exposure timing at Tor

8 at the Pukerangi location overlaps MIS 5, MIS 4 (71–57 ka) and MIS 3 (57–29 ka). The MIS 5 is, together with MIS 11, one of the wettest and warmest periods of the last 800 ka (Past Interglacials Working Group of PAGES, 2016). Thus, the age of increases and peak phases recorded by Tor 1, 2, 5 and 8 appear to coincide with warmer and more humid periods. In summary the TEA indicates that most tors at the study sites were exhumed in the warm period of MIS 5 (~130–71 ka), potentially as a result of higher surface denudation rates during this warmer and more humid time.

5.5. Potential relation of tor exposure and surface uplift

Modern vertical tectonic movements for the southeast of New Zealand have been estimated at 0–1 [m kyr⁻¹] (Fig. 1b) by McSaveney and Nathan (2006). South Rough Ridge is thought to have experienced ~60 m of uplift over the last ~550 ka, at a rate of 0.10 ± 0.02 [m kyr⁻¹] (Bennett et al., 2006). Holocene rock uplift rates near Moonlight Flat (Fig. 2) are between 0.43 and 0.68 [m kyr⁻¹]. The long-term Quaternary uplift rates of the Taieri Fault are about 0.02 [m kyr⁻¹], interspersed with episodic uplift periods up to 0.35 [m kyr⁻¹] (Nicolls, 2020).

Comparing the diverse rock uplift rates (U_R) above to the TEA derived $D_{Surface}$ rate maxima in this study, allows a better understanding of actual surface uplift rates (U_S ; see Table S1). The average lows in tors in this study are around 0.01–0.02 [m kyr⁻¹], which is equivalent to the Quaternary average exhumation rate (U_E) of 0.02 [m kyr⁻¹]

A

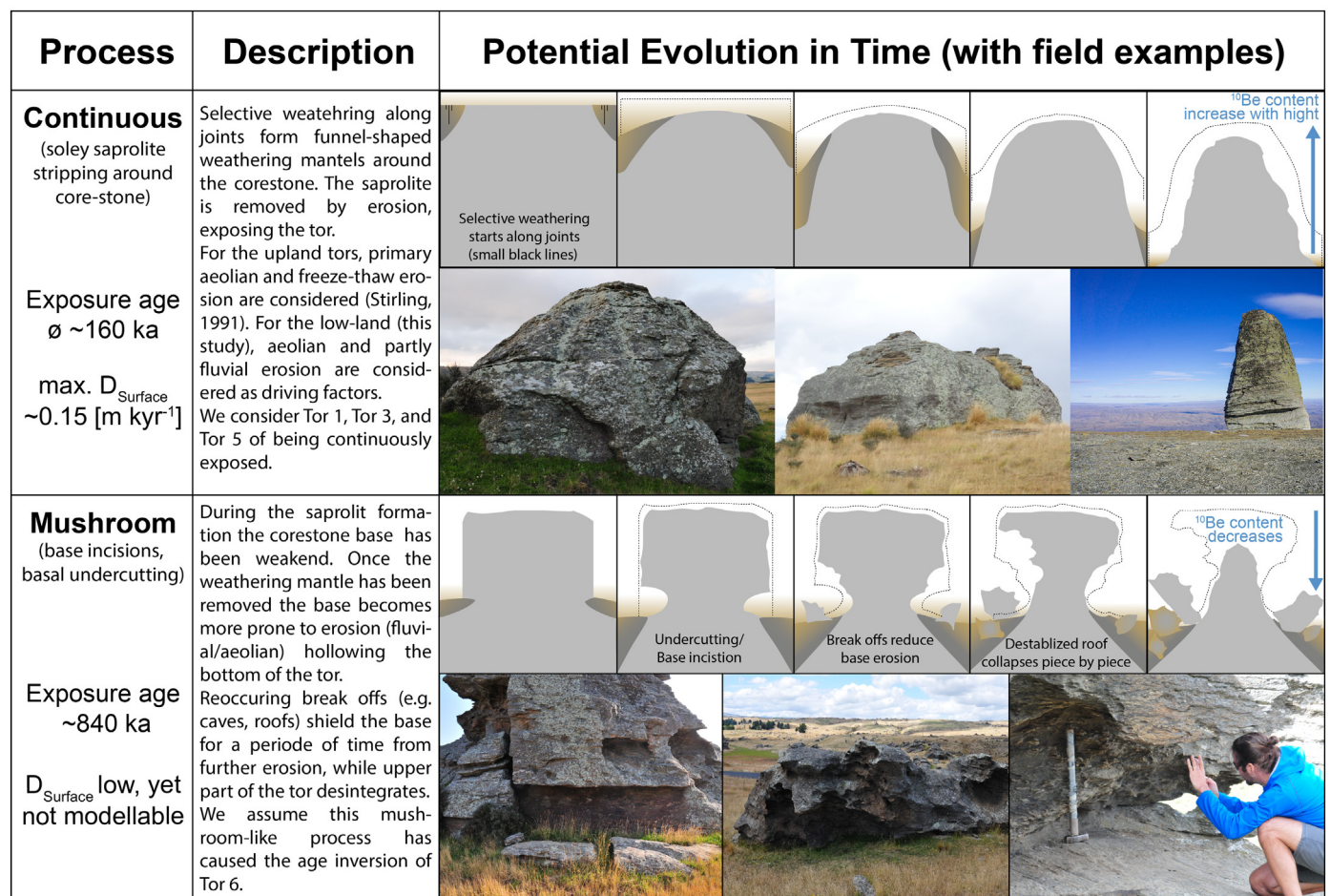


Fig. 8. (Part A & B) Conceptual models with accompanying field photographs of the four most common schist tor evolutions in East Otago. Variations and combinations of these patterns can occur. The surface degradation differences after each time-interval are represented with dotted lines. Light grey represents the meta-sedimentary schist rock. The grey to brown gradient represents the potential weathering mantle. The light brown represents the eventual soil cover. The tilted dashed lines in panel four (structural) represent the dominant schistosity.

B

Process	Description	Potential Evolution in Time (with field examples)					
Tafoni (hollowing out) Exposure age $\varnothing \sim 210$ ka max. D_{Surface} ~ 0.04 [m kyr ⁻¹]	Once the tor has surfaced, wind erosion starts hollowing the surface. The hollowing of the tor progresses with further exposure of the tor. The tafonis weaken the stability of the internal structure, until (parts of) cave(s) collapse. Besides aeolian erosion, also wind-driven evaporation and salt encrustations are considered as tafoni forming factors. These irreconstructable process, potential caused most age inversions e.g. Tor 4, Tor 2.						
Structural (failure planes, sliding, falling) Exposure age $\varnothing \sim 120$ ka max. D_{Surface} ~ 0.12 [m kyr ⁻¹]	Local tors are dominated by sub-vertical jointing and sub-horizontal schistosity (Fahey, 1981). The inherent internal structure of schist tors is therefore an additional decomposing factor during the removal of the stabilizing weathering mantle. We have seen failure planes parallel to the schistosity as well as block separations and break-off parallel to jointing. The process appear to be responsible for the younger ages of ~, Tor 8 (~22 ka) and Tor 7 (~20 ka).						

Fig. 8 (continued).

found by Nicolls (2020) on the Taieri Fault. Episodic increased uplift on the Taieri Fault would cause a resultant increase in D_{Surface} rates, which we estimate to be ~ 0.13 – 0.25 [m kyr⁻¹] (Table S1). We suggest that the current denudation rates are probably somewhere between the tor-based maxima of ~ 0.22 [m kyr⁻¹] and the modern soil erosion rates low of 0.48 [m kyr⁻¹] (for example see rates by Hewitt, 1996; chapter 5.2). The subsequent difference would result in an U_s rate of ~ 0.21 to ~ 0.64 [m kyr⁻¹]. Based on this, our preferred interpretation is that the East Otago surface experienced general Quaternary uplift rates of ~ 0.01 [m kyr⁻¹]. Although these rates are in agreement with other studies (Nicolls, 2020; McSaveney and Nathan, 2006), we note that our investigation was carried out in an area where the landscape has been/is being uplifted by relatively small amounts compared to the substantially uplifted mountains of West Otago. In general, the long-term erosion rates are low, so that much of the topography is constructional via differential tectonic uplift rather than erosional in origin (Koons, 1995). Hence, the region is principally controlled by plate boundary tectonics associated with, for example, the Alpine Fault, yet individual topographic features (e.g. Rock and Pillar Range, Taieri Ridge or Billys Ridge) are the result of sub-ordinate faults and shear zones (e.g. Hyde Fault, Taieri Ridge Faults; see Craw et al., 2016). For our investigated geomorphic zone in East Otago, the effective U_s commenced decreasing during the Middle Pleistocene (Chibanian) from about 0.04 – 0.09 [m kyr⁻¹] to ~ 0.01 [m kyr⁻¹]. This decrease was possibly followed by a strong increase in uplift rate during the Holocene to potentially 0.21 – 0.64 [m kyr⁻¹] (Fig. 9 and Fig. S1).

6. Conclusions

The tor exhumation approach (TEA) enables quantification of surface lowering and, thus, denudation rates (D_{Surface}). This approach has been applied so far only for granitic landscapes. Schist rocks have a clear anisotropy that appear to lead to a different physical and chemical weathering trend. This results in a more complex emergence from the topographic surface relative to granite tor landscapes. Surface denudation models had to be adjusted to the individual surface exposure age profiles of the tors. The models are the results of simulations within the age variations of the acceptable surface ages. The tors at three locations (valley, ridge, distal) of East Otago on the South Island of New Zealand record different exposure and surface denudation trends. They also exhibit a mix of exposure process patterns (e.g. continuous, mushroom, tafoni, structural).

The distal location revealed a mostly continuous exposure history for about 120 ka and D_{Surface} rates of ~ 0.2 to 0.03 [m kyr⁻¹]. Tors at the valley location show D_{Surface} rates of ~ 0.22 [m kyr⁻¹] to ~ 0.02 [m kyr⁻¹] commencing 30 ka earlier than the distal location at ~ 100 m lower altitude. In contrast, the surface denudation rates of the ridge resulted in lower values of mostly ~ 0.03 [m kyr⁻¹], with the exception of the ridge crest, where alternative models indicate rates of up to 0.3 [m kyr⁻¹]. In addition, a clear age inversion of one tor (subsurface age of ~ 800 ka, top age ~ 200 ka) is probably the result of undercut (mushroom-like) exposure. The ridge appears to have been exposed approximately 30 ka earlier than the valley located 150 m below. Tors that

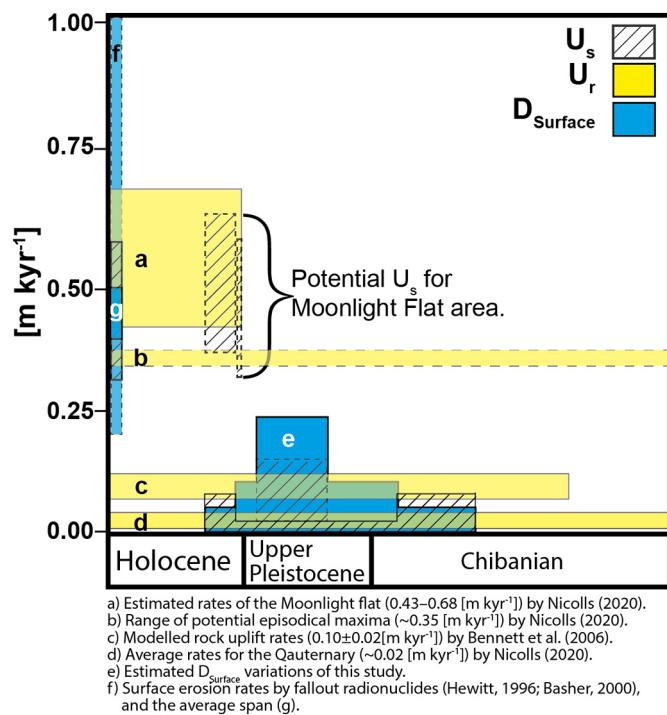


Fig. 9. Estimated Quaternary surface uplift (U_s) variations using tor derived surface denudation rates ($D_{Surface}$). Note that McSaveney and Nathan (2006) estimate the U_s to be around 0–1 [m kyr⁻¹], although rock uplifts (U_r) are in general found to be lower. In detail: (a) Estimated rates of the Moonlight flat (0.43–0.68 [m kyr⁻¹]) by Nicolls (2020). (b) Range of potential episodic maxima (~0.35 [m kyr⁻¹]) by Nicolls (2020). (c) Modelled rock uplift rates (0.10 ± 0.02 [m kyr⁻¹]) by Bennett et al. (2006). (d) Average rates for the Quaternary (~0.02 [m kyr⁻¹]) by Nicolls (2020). (e) Estimated $D_{Surface}$ variations of this study. (f) Surface erosion rates by fallout radionuclides (Hewitt, 1996; Basher, 2000), and the average span (g). A split data presentation is found in Fig. S1.

underwent a partial self-protective process (e.g. mushroom, tafoni exposure), resulted in the oldest surface ages and lowest $D_{Surface}$ rates. A comparison of the long-term tor derived rates with modern soil erosion data (¹³⁷Cs) indicates that surface erosion rates distinctly increased at the ridge location during the last few decades. This is mainly caused by anthropogenic impact.

The current study shows a non-linear and complex surface evolution of East Otago during the Holocene and Pleistocene. This variability is partially related to varying climatic conditions with the highest surface denudation phases coincident with the wet and warm MIS 5 (130–71 ka). Overall, uplift rates started to exceed surface lowering rates at the onset of the Holocene. The driving mechanism of denudation and tor exposure of East Otago is a synergy of climate and tectonic uplift.

Supplementary data to this article can be found online at <https://doi.org/10.1016/j.geomorph.2021.107849>.

Declaration of competing interest

The authors declare that they have no known competing financial interests or personal relationships that could have appeared to influence the work reported in this paper.

Acknowledgement

This research was supported by the Swiss National Science Foundation (SNSF) project grant no. 200021_162338/1. Special thanks go to the master students Aidan McLean and Martin Harms. Kevin Patrick Norton was supported by a SNSF Visiting International Fellowship (IZK022_170715/1) and the Royal Society Te Apārangi Rutherford Discovery Fellowship. Gerald Raab was supported by the Forschungskredit of the University of

Zürich FK-19-108. We thank Dave Craw and one anonymous reviewer for comments, and Martin Stokes for editorial handling.

References

- Adams, C.J., Campbell, H.J., Griffin, W.L., 2007. Provenance comparisons of Permian to Jurassic tectonostratigraphic terranes in New Zealand: perspectives from detrital zircon age patterns. *Geol. Mag.* 144, 701–729.
- Adams, C.J., Campbell, H.J., Griffin, W.L., 2009. Tracing the Caples Terrane through New Zealand Using Detrital Zircon Age Patterns and Radiogenic Isotope Signatures (New Zealand).
- Balco, G., Stone, J.O., Lifton, N.A., Dunai, T.J., 2008. A complete and easily accessible means of calculating surface exposure ages or erosion rates from ¹⁰Be and ²⁶Al measurements. *Quat. Geochronol.* 8, 174–195. <https://doi.org/10.1016/j.quageo.2007.12.001>.
- Barrell, D.J.A., 2011. Quaternary glaciers of New Zealand. *Developments in Quaternary Sciences*. vol. 15, pp. 1047–1064.
- Basher, L.R., 2000. Surface erosion assessment using ¹³⁷Cs: examples from New Zealand. *Acta Geol. Hisp.* 35, 219–228.
- Basher, L.R., 2010. Effects of mass-movement erosion. *Manaaki Whenua – Landcare Research, Soil Horizon Newsletter Issue*. vol. 19.
- Bennett, E., Youngson, J., Jackson, J., Norris, R., Raisbeck, G., Yiou, F., 2006. Combining morphological observations with in situ cosmogenic isotope measurements to study anticline growth and fault propagation in Central Otago, New Zealand. *N. Z. J. Geol. Geophys.* 49 (2), 217–231. <https://doi.org/10.1080/00288306.2006.9515161>.
- Borchers, B., Marrero, S., Balco, G., Caffee, M., Goehring, B., Lifton, N., Nishiizumi, K., Phillips, F., Schaefer, J., Stone, J., 2016. Geological calibration of spallation production rates in the CRONUS-Earth. *Quat. Geochronol.* 31, 188–198. <https://doi.org/10.1016/j.quageo.2015.01.009>.
- Brown, E.H., 1963. The geology of the Mt Stoker area, Eastern Otago. *N. Z. J. Geol. Geophys.* 6 (5), 847–871.
- Brown, E.H., 1967. The greenschist facies in part of eastern Otago, New Zealand. *Contrib. Mineral. Petrol.* 14 (4), 259–292.
- Brown, E.H., 1968. Metamorphic structures in part of the Eastern Otago Schists. *N. Z. J. Geol. Geophys.* 11, 41–65.
- Brown, E.T., Edmond, J.M., Raisbeck, G.M., Yiou, F., Desgarceaux, S., 1992. Effective attenuation length of cosmic rays producing ¹⁰Be and ²⁶Al in quartz: implications for surface exposure dating. *Geophys. Res. Lett.* 9, 369–372. <https://doi.org/10.1029/92GL00266>.
- Calcaterra, D., Parise, M., 2010. Weathering as a predisposing factor to slope movements: an introduction. *Geol. Soc. Lond. Eng. Geol. Spec. Publ.* 23 (1), 1–4.
- Campbell, J.D., Warren, G., 1965. Fossil localities of the Torlesse Group in the South Island. *Trans. R. Soc. N. Z.* 3, 99–137.
- Chamberlain, C.P., Poage, M.A., Craw, D., Reynolds, R.C., 1999. Topographic development of the Southern Alps recorded by the isotopic composition of authigenic clay minerals, South Island, New Zealand. *Chem. Geol.* 155 (3–4), 279–294. [https://doi.org/10.1016/S0009-2541\(98\)00165-X](https://doi.org/10.1016/S0009-2541(98)00165-X).
- Chmeleff, J., von Blanckenburg, F., Kossert, K., Jakob, D., 2010. Determination of the ¹⁰Be half-life by multicollector ICP-MS and liquid scintillation counting. *Nucl. Instrum. Methods Phys. Res., Sect. B* 268, 192–199. <https://doi.org/10.1016/j.nimb.2009.09.012>.
- Christl, M., Vockenhuber, C., Kubik, P.Q., Wacker, L., Lachner, J., Alfimov, V., Synal, H.A., 2013. The ETH Zurich AMS facilities: performance parameters and reference materials. *Nucl. Inst. Methods Phys. Res. B* 294, 29–38. <https://doi.org/10.1016/j.nimb.2012.03.004>.
- Cossens, G.G., 1987. Agriculture and climate in Central Otago. *Proceedings of the New Zealand Grassland Association*. vol. 48, pp. 15–21.
- Craw, D., 2013. River drainage reorientation during placer gold accumulation, southern New Zealand. *Mineral. Deposita* 48 (7), 841–860.
- Craw, D., Beckett, S., 2004. Water and sediment chemistry of Sutton Salt Lake, east Otago, New Zealand. *N. Z. J. Mar. Freshw. Res.* 38, 315–328.
- Craw, D., Kerr, G., 2017. Geochemistry and mineralogy of contrasting supergene gold alteration zones, southern New Zealand. *Appl. Geochem.* 85, 19–34.
- Craw, D., MacKenzie, D., Grieve, P., 2015. Supergene gold mobility in orogenic gold deposits, Otago Schist, New Zealand. *N. Z. J. Geol. Geophys.* 58 (2), 123–136. <https://doi.org/10.1080/00288306.2014.997746>.
- Craw, D., Craw, L., Burrige, C., Wallis, G., Waters, J., 2016. Evolution of the Taieri River catchment, East Otago, New Zealand. *N. Z. J. Geol. Geophys.* 59, 257–273.
- Ehlen, J., 1992. Analysis of spatial relationships among geomorphic, petrographic and structural characteristics of the Dartmoor tors. *Earth Surf. Process. Landf.* 17 (1), 53–67.
- Evans, D.J., Kalyan, R., Orton, C., 2017. Periglacial geomorphology of summit tors on Bodmin Moor, Cornwall, SW England. *J. Maps* 13 (2), 342–349.
- Fahey, B.D., 1981. Origin and age of upland schist tors in Central Otago, New Zealand. *N. Z. J. Geol. Geophys.* 24 (3), 399–413.
- Fahey, B.D., 1986. Weathering pit development in the Central Otago mountains of southern New Zealand. *Arct. Alp. Res.* 18 (3), 337–347.
- Forster, M.A., Lister, G.S., 2003. Cretaceous metamorphic core complex in the Otago Schist, New Zealand. *Aust. J. Earth Sci.* 50 (2), 181–198. <https://doi.org/10.1046/j.1440-0952.2003.00986.x>.
- Gibbons, C.L.M.H., 1981. Tors in Swaziland. *Geogr. J.* 72–78.
- Goodfellow, B.W., Skelton, A., Martel, S.J., Stroeven, A.P., Jansson, K.N., Hättetrand, C., 2014. Controls of tor formation, Cairngorm Mountains, Scotland. *J. Geophys. Res. Earth Surf.* 119 (2), 225–246.

- Gosse, J.C., Philips, F.M., 2001. Terrestrial in situ produced cosmogenic nuclides: theory and application. *Quat. Sci. Rev.* 20, 1475–1560. [https://doi.org/10.1016/S0277-3791\(00\)00171-2](https://doi.org/10.1016/S0277-3791(00)00171-2).
- Gray, D.R., Foster, D.A., 2004. 40Ar/39Ar thermochronologic constraints on deformation, metamorphism and cooling/exhumation of a Mesozoic accretionary wedge, Otago Schist, New Zealand. *Tectonophysics* 385, 181–210.
- Gunnell, Y., Jarman, D., Braucher, R., Calvet, M., Delmas, M., Leanni, L., Bourles, D., Arnold, M., Aumaitre, G., Keddaouche, K., 2013. The granite tors of Dartmoor, Southwest England: rapid and recent emergence revealed by Late Pleistocene cosmogenic apparent exposure ages. *Quat. Sci. Rev.* 61, 62–76.
- Hall, A.M., Migoñ, P., 2010. The first stages of erosion by ice sheets: evidence from central Europe. *Geomorphology* 123 (3–4), 349–363.
- Hall, A.M., Sarala, P., Ebert, K., 2015. Late Cenozoic deep weathering patterns on the Fennoscandian shield in northern Finland: a window on ice sheet bed conditions at the onset of Northern Hemisphere glaciation. *Geomorphology* 246, 472–488.
- Hatherton, T., Leopold, A., 1964. The densities of New Zealand rocks. *N. Z. J. Geol. Geophys.* 7 (3), 605–625.
- Hättestrand, C., Stroeven, A.P., 2002. A relict landscape in the centre of Fennoscandian glaciation: geomorphological evidence of minimal Quaternary glacial erosion. *Geomorphology* 44 (1–2), 127–143.
- Heimsath, A.M., Chappell, J., Dietrich, W.E., Nishiizumi, K., Finkel, R.C., 2001. Late Quaternary erosion in southeastern Australia: a field example using cosmogenic nuclides. *Quat. Int.* 83, 169–185.
- Hewitt, A.E., 1996. Estimating surface erosion using ¹³⁷Cs at a semi-arid site in Central Otago, New Zealand. *J. R. Soc. N. Z.* 26 (1), 107–118.
- Jackson, J., Ritz, J.F., Siame, L., Raisbeck, G., Yiou, F., Norris, R., Youngson, J., Bennett, E., 2002. Fault growth and landscape development rates in Otago, New Zealand, using in situ cosmogenic ¹⁰Be. *Earth Planet. Sci. Lett.* 195, 185–193.
- Jugum, D., Norris, R.H., Palin, J.M., 2013. Late Jurassic detrital zircons from the Haast Schist and their implications for New Zealand terrane assembly and metamorphism. *N. Z. J. Geol. Geophys.* 56, 223–228.
- Kim, K.J., Englert, P.A.J., 2004. Profiles of in situ ¹⁰Be and ²⁶Al at great depths at the Macraes Falt, East Otago, New Zealand. *Earth Planet. Sci. Lett.* 223, 113–126.
- Kitchener, J.A., 1984. The froth flotation process: past, present and future – in brief. In: Ives, K.J. (Ed.), *The Scientific Basis of Flotation*. NATO ASI Series (Series E: Applied Sciences). Springer, Dordrecht, p. 75. https://doi.org/10.1007/978-94-009-6926-1_2.
- Kohl, C., Nishiizumi, K., 1992. Chemical isolation of quartz for measurement of in-situ-produced cosmogenic nuclides. *Geochim. Cosmochim. Acta* 56, 3583–3587. [https://doi.org/10.1016/0016-7037\(92\)90401-4](https://doi.org/10.1016/0016-7037(92)90401-4).
- Koons, P.O., 1995. Modeling the topographic evolution of collisional belts. *Annu. Rev. Earth Planet. Sci.* 23 (1), 375–408.
- Korschinek, G., Bergmaier, A., Faestermann, T., Gerstmann, U.C., Remmert, A., 2010. A new value for the half-life of ¹⁰Be by heavy-ion elastic recoil detection and liquid scintillation counting. *Nucl. Instrum. Methods Phys. Res., Sect. B* 268, 187–191. <https://doi.org/10.1016/j.nimb.2009.09.020>.
- Kubik, P.W., Christl, M., 2010. ¹⁰Be and ²⁶Al measurements at the Zurich 6 MV Tandem AMS facility. *Nucl. Instrum. Methods Phys. Res., Sect. B* 268 (7–8), 880–883.
- Lichter, J., 1998. Rates of weathering and chemical depletion in soils across a chronosequence of Lake Michigan sand dunes. *Geoderma* 85, 255–282. [https://doi.org/10.1016/S0016-7061\(98\)00026-3](https://doi.org/10.1016/S0016-7061(98)00026-3).
- Linton, D.L., 1955. The problem of tors. *Geogr. J.* 121 (4), 470–487.
- Lisiecki, L.E., Raymo, M.E., 2005. A Pliocene-Pleistocene stack of 57 globally distributed benthic $\delta^{18}\text{O}$ records. *Paleoceanography* 20 (1).
- Litchfield, N.J., Lian, O.B., 2004. Luminescence age estimates of Pleistocene marine terrace and alluvial fan sediments associated with tectonic activity along coastal Otago, New Zealand. *N. Z. J. Geol. Geophys.* 47 (1), 29–37.
- Little, T.A., Mortimer, N., McWilliams, M., 1999. An episodic Cretaceous cooling model for the Otago-Marlborough Schist, New Zealand, based on 40Ar/39Ar white mica ages. *N. Z. J. Geol. Geophys.* 42, 305–325.
- Martin, A.P., Rattenbury, M.S., Cox, S.C., 2013. Geophysics-aided geological interpretation of the Otago Schist: new insights for mineral exploration and geological mapping. In: Taylor, J. (convener), *Australasian Institute of Mining and Metallurgy New Zealand Branch Annual Conference on Exploration, Mining and New Zealand's Mineral Resources*, 2013, Nelson, pp. 307–315.
- Martin, A.P., Turnbull, R.E., Rattenbury, M.S., Cohen, D.R., Hoogewerf, J., Rogers, K.M., Baisden, W.T., Christie, A.B., 2016a. The regional geochemical baseline soil survey of southern New Zealand: design and initial interpretation. *J. Geochem. Explor.* 167, 70–82.
- Martin, A.P., Cox, S.C., Smith Lyttle, B., 2016b. *Geology of the Middlemarch area 1:50 000. GNS Science Geological Map 5. GNS Science, Lower Hutt, New Zealand.*
- Masarik, J., Frank, M., Schaefer, J.M., Wieler, R., 2001. Correction of in-situ cosmogenic nuclide production rates for geomagnetic field intensity variations during the past 800,000 years. *Geochim. Cosmochim. Acta* 65, 2995–3003.
- Maunder, W.J., 1965. Climatic character. In: Lister, R.G. (Ed.), *Central Otago*. Ibid, p. 195.
- McGlone, M.S., 1983. Polynesian deforestation of New Zealand: a preliminary synthesis. *Archaeol. Ocean.* 18, 11–25.
- McGowan, H.A., Sturman, A.P., 1996. Regional and local scale characteristics of foehn wind events over the South Island of New Zealand. *Meteorol. Atmos. Phys.* 58 (1–4), 151–164.
- McGowan, H.A., Sturman, A.P., Kossmann, M., Zawar-Reza, P., 2002. Observations of foehn onset in the Southern Alps, New Zealand. *Meteorol. Atmos. Phys.* 79 (3), 215–230.
- McSaveney, E., Nathan, E., 2006. *Geology – overview – Holocene – the last 10,000 years'*. Te Ara – the Encyclopedia of New Zealand. <http://www.TeAra.govt.nz/en/map/8406/uplift-of-new-zealand>.
- McWethy, D.B., Whitlock, C., Wilmschurst, J.M., McGlone, M.S., Li, X., 2009. Rapid deforestation of South Island, New Zealand, by early Polynesian fires. *Holocene* 19, 883–897.
- Michniewicz, A., 2019. Tors in Central European Mountains—are they indicators of past environments? *Bull. Geogr. Phys. Geogr. Ser.* 16 (1), 67–87.
- Migoñ, P., 2006. *Granite Landscapes of the World*. vol. 2. Oxford University Press.
- Migoñ, P., 2020. Geomorphology of conglomerate terraces – global overview. *Earth-Sci. Rev.* 208, 10302. <https://doi.org/10.1016/j.earscirev.2020.103302>.
- Mortimer, N., 2000. Metamorphic discontinuities in orogenic belts: example of the garnet–biotite–albite zone in the Otago Schist, New Zealand. *Int. J. Earth Sci.* 89, 295–306.
- Mortimer, N., 2004. New Zealand's geological foundations. *Gondwana Res.* 7 (1), 261–272.
- Mortimer, N., Cooper, A.F., 2004. U–Pb and Sm–Nd ages from the Alpine Schist, New Zealand. *N. Z. J. Geol. Geophys.* 47 (1), 21–28.
- Mortimer, N., Roser, B.P., 1992. Geochemical evidence for the position of the Caples–Torlesse boundary in the Otago Schist, New Zealand. *J. Geol. Soc.* 149, 967–977.
- Mortimer, N., McLaren, S., Dunlap, W.J., 2012. Ar–Ar dating of K-feldspar in low grade metamorphic rocks: example of an exhumed Mesozoic accretionary wedge and forearc, South Island, New Zealand. *Tectonics* 32, 1–15.
- Nicolls, R., 2020. *Tectonic Geomorphology of the Rock and Pillar Range and Taieri Ridge, Otago, New Zealand* (Thesis, Master of Science). University of Otago Retrieved from. <http://hdl.handle.net/10523/10077>.
- Nishiizumi, K., Imamura, M., Caffee, M.W., Southon, J.R., Finkel, R.C., McAnich, J., 2007. Absolute calibration of ¹⁰Be AMS standards. *Nucl. Instrum. Methods Phys. Res., Sect. B* 258, 403–413. <https://doi.org/10.1016/j.nimb.2007.01.297>.
- Norris, R.J., 2004. Strain localization within ductile shear zones beneath active faults: the Alpine Fault contrasted with the adjacent Otago Fault system, New Zealand. *Earth Planets Space* 56, 1095–1101.
- Ollier, C.D., 2010. Very deep weathering and related landslides. *Geol. Soc. Lond. Eng. Geol. Spec. Publ.* 23, 5–14. <https://doi.org/10.1144/EGSP23.2>.
- Past Interglacials Working Group of PAGES, 2016. Interglacials of the last 800,000 years. *Rev. Geophys.* 54 (1), 162–219.
- Peizhen, Z., Molnar, P., Downs, W., 2001. Increased sedimentation rates and grain sizes 2–4 Myr ago due to the influence of climate change on erosion rates. *Nature* 410, 891–897. <https://doi.org/10.1038/35073504>.
- Pigati, J.S., Lifton, N.A., 2004. Geomagnetic effects on time-integrated cosmogenic nuclide production with emphasis on in situ ¹⁴C and ¹⁰B. *Earth Planet. Sci. Lett.* 226, 193–205. <https://doi.org/10.1016/j.epsl.2004.07.031>.
- Portes, R., Dahms, D., Brandová, D., Raab, G., Christl, M., Kühn, P., Ketterer, M., Egli, M., 2018. Evolution of soil erosion rates in alpine soils of the Central Rocky Mountains using fallout Pu and $\delta^{13}\text{C}$. *Earth Planet. Sci. Lett.* 496, 258–269. <https://doi.org/10.1016/j.epsl.2018.06.002>.
- Putnam, A.E., Schaefer, J.M., Barrell, D.J.A., Vandergoes, M., Denton, G.H., Kaplan, M.R., Finkel, R.C., Schwartz, R., Goehring, B.M., Kelley, S.E., 2010. In situ cosmogenic ¹⁰Be production-rate calibration from the Southern Alps, New Zealand. *Quat. Geochronol.* 5–4, 392–409.
- Raab, G., 2019. *The Tor Exhumation Approach – A New Technique to Derive Continuous In-Situ Soil Erosion and Surface Denudation Models*. PhD Dissertation. University of Zürich, Switzerland <https://doi.org/10.13140/RG.2.2.29904.87043>.
- Raab, G., Scarciglia, F., Norton, K., Dahms, D., Brandová, D., de Castro Portes, R., Christl, M., Kletterer, M.E., Ruppli, A., Egli, M., 2018. Denudation variability of the Sila Massif upland (Italy) from decades to millennia using ¹⁰Be and ²³⁹⁺²⁴⁰Pu. *Land Degrad. Dev.* 29, 3736–3752. <https://doi.org/10.1002/ldr.3120>.
- Raab, G., Egli, M., Norton, K., Dahms, D., Brandová, D., Christl, M., Scarciglia, F., 2019. Climate and relief-induced controls on the temporal variability of denudation rates in a granitic upland. *Earth Surf. Process. Landf.* 44 (13), 2570–2586. <https://doi.org/10.1002/esp.4681>.
- Raeside, J.D., 1949. The origin of schist tors in central Otago. *N. Z. Geogr.* 5 (1), 72–76.
- Rees-Jones, J., Rink, W.J., Norris, R.J., Litchfield, N.J., 2000. Optical luminescence dating of uplifted marine terraces along the Akatore Fault near Dunedin, South Island, New Zealand. *N. Z. J. Geol. Geophys.* 43 (3), 419–424.
- Roche, M., 1994. *Land and Water: Water and Soil Conservation and Central Government in New Zealand 1941–1988*. Historical Branch, Department of Internal Affairs, Wellington.
- Scarciglia, F., Le Pera, E., Critelli, S., 2005. Weathering and pedogenesis in the Sila Grande Massif (Calabria, south Italy): from field scale to micromorphology. *Catena* 61, 1–29. <https://doi.org/10.1016/j.catena.2005.02.001>.
- Stirling, M.W., 1990. The Old Man Range and Garvie Mountains: tectonic geomorphology of the Central Otago peneplain, New Zealand. *N. Z. J. Geol. Geophys.* 33 (2), 233–243.
- Stirling, M.W., 1991. Peneplain modification in an alpine environment of Central Otago, New Zealand. *N. Z. J. Geol. Geophys.* 34 (2), 195–201.
- Stolt, M.H., Baker, J.C., 1994. Strategies for studying saprolite and saprolite genesis. *Whole Regolith Pedology*. vol. 34, pp. 1–19.
- Stolt, M.H., Baker, J.C., Simpson, T.W., 1991. Micromorphology of the soil-saprolite transition zone in Hapludults of Virginia. *Soil Sci. Soc. Am. J.* 55 (4), 1067–1075.
- Stone, J.O., 2000. Air pressure and cosmogenic isotope production. *J. Geophys. Res.* 105, 753–759. <https://doi.org/10.1029/2000JB900181>.
- Suggate, R.P., 1961. Rock-stratigraphic names for the South Island schists and undifferentiated sediments of the New Zealand geosyncline. *N. Z. J. Geol. Geophys.* 4, 392–399.
- Turnbull, I. M. (compiler) 2000. *Geology of the Wakatipu Area*. Institute of Geological and Nuclear Sciences 1:250 000 geological map 18. Lower Hutt, Institute of Geological and Nuclear Sciences Ltd.
- Turnbull, I.M., Mortimer, N., Craw, D., 2001. Textural zones in the Haast Schist—a reappraisal. *N. Z. J. Geol. Geophys.* 44, 171–183.
- Turner, F.J., 1952. "Gefuegerelief" illustrated by "schist tor" topography in central Otago, New Zealand. *Am. J. Sci.* 250 (11), 802–807.
- Vidal Romaní, J.R., 2008. *Forms and Structural Fabric in Granite Rocks*.

- von Blanckenburg, F., Belshaw, N.S., O'Nions, R.K., 1996. Separation of ^9Be and cosmogenic ^{10}Be from environmental materials and SIMS isotope dilution analysis. *Chem. Geol.* 129, 93–99. [https://doi.org/10.1016/0009-2541\(95\)00157-3](https://doi.org/10.1016/0009-2541(95)00157-3).
- Weinberger, R., Eyal, Y., Mortimer, N., 2010. Formation of systematic joints in metamorphic rocks due to release of residual elastic strain energy, Otago Schist, New Zealand. *J. Struct. Geol.* 32, 288–305.
- West, J., 2017. *The Face of Nature: An Environmental History of the Otago Peninsula*. Otago University Press.
- Wittmann, H., von Blanckenburg, F., Kruesmann, T., Norton, K.P., Kubik, P.W., 2007. Relation between rock uplift and denudation from cosmogenic nuclides in river sediment in the Central Alps of Switzerland. *J. Geophys. Res. Earth Surf.* 112 (F4).
- Wood, B.L., 1969. Periglacial topography in southern New Zealand. *N. Z. J. Geol. Geophys.* 12 (2–3), 361–375.
- Youngson, J., Bennett, E., Jackson, J., Norris, R., Raisbeck, G., Yiou, F., 2005. “Sarsen Stones” at German Hill, Central Otago, New Zealand, and their potential for in situ cosmogenic isotope dating of landscape evolution. *J. Geol.* 113, 341–354.
- Zollinger, B., Alewell, C., Kneisel, C., Meusbürger, K., Brandová, D., Kubik, P., Schaller, M., Ketterer, M., Egli, M., 2015. The effect of permafrost on time-split soil erosion using radionuclides (^{137}Cs , $^{239+240}\text{Pu}$, meteoric ^{10}Be) and stable isotopes ($\delta^{13}\text{C}$) in the eastern Swiss Alps. *J. Soils Sediments* 15 (6), 1400–1419. <https://doi.org/10.1007/s11368-014-0881-9>.